JOURNAL OF GEOPHYSICAL RESEARCH, VOL. 108, NO. E9, 5097, doi:10.1029/2003JE002057, 2003

Constraints on the size of Martian aerosols from Thermal Emission Spectrometer observations

Michael J. Wolff and R. Todd Clancy
Space Science Institute, Boulder, Colorado, USA

Received 5 February 2003; revised 23 April 2003; accepted 6 May 2003; published 3 September 2003.

[1] We combine a robust multiple-scattering radiative transfer algorithm with the Thermal Emission Spectrometer (TES) spectral data set in order to characterize the properties of Martian aerosol particles. Because of the importance of accurate model input when performing such retrievals, we include self-consistent and physically plausible treatments of surface emissivity and atmospheric aerosol dielectric functions, as well as gaseous absorption effects. Considerable effort is expended in the identification and discussion of potential sources of error and uncertainty. Significant results stemming from this analysis are a new dust aerosol dielectric function that appears to well represent the IR spectral behavior sampled by TES for a wide range of dust loading conditions, two distinct populations of water ice particles with r_{eff} of $\sim$1–2 μm and $\sim$3–4 μm; and distinct departures in dust particle sizes during the 2001A global dust storm from the canonical 1.6–1.7 μm values. Very consistent aerosol size distributions are obtained when 9 μm dust and 12 μm ice optical depths retrieved from this analysis are compared to visible optical depths retrieved from TES solar band emission phase function sequences [*Clancy et al.*, 2003]. Direct comparison of our optical depths to those available from the Planetary Data System (PDS) (as provided by the TES science team) reveals a systematic bias toward τ values which are 20–30% (or more) too small. Much of this offset stems from the fact that TES PDS aerosol optical depths are actually an approximation to $\tau_{absorption}$, which is $\sim$30% lower than $\tau_{extinction}$ for Mars dust aerosols. Additional biases in TES optical depths arise from assumptions of fixed surface emissivity and temperature. *INDEX TERMS:* 0305 Atmospheric Composition and Structure: Aerosols and particles (0345, 4801); 0360 Atmospheric Composition and Structure: Transmission and scattering of radiation; 6225 Planetology: Solar System Objects: Mars; *KEYWORDS:* Martian atmosphere, aerosols, radiative transfer, remote sensing, thermal emission spectrometer

Citation: Wolff, M. J., and R. T. Clancy, Constraints on the size of Martian aerosols from Thermal Emission Spectrometer observations, *J. Geophys. Res.*, *108*(E9), 5097, doi:10.1029/2003JE002057, 2003.

1. Introduction

[2] The importance of aerosols in the behavior and evolution of the Martian atmosphere and its weather systems was recognized even prior to the arrival of Mariner 9 at Mars [e.g., *Gierasch and Goody*, 1972]. Naturally, quantifying the exact role played by such particles in the atmosphere was, and continues to be, a topic of considerable interest, particularly with respect to the use of Mars Global Circulation Models (MCGMs) to reproduce observed atmospheric phenomena. As a consequence, one requires knowledge about the radiative properties of the particles: e.g., single scattering albedo, asymmetry parameter, electromagnetic scattering cross sections. While the aforementioned characteristics are those used explicitly by radiative transfer algorithms, the general dearth of directly relevant laboratory measurements necessitates the application of numerical models of aerosol scattering properties as constrained by retrievals of microphysical properties: e.g., size, composition (dust versus water ice), shape. The first two quantities in the list are very fundamental in terms of aerosol interactions with the Martian atmosphere. The role of aerosols in atmospheric radiative balance is essentially a function of forward-scattering quantities, which typically have a weak dependence on particle shape. Changes, as well as errors and large uncertainties, in either size or composition can produce significant differences in the radiative properties of the particles. For example, the single scattering albedo of otherwise identical dust and water ice aerosols can be substantially different in both the visible and near infrared (IR) (e.g., 0.3–3 μm), where effectively all of the solar insolation absorption by aerosols occurs. Furthermore, a change in average particle size from 1.0 to 1.5 μm or from 1.5 to 2 μm will change the optical-to-visible opacity ratio by 20–30% or more (depending on shape and the width of the distribution [see *Clancy et al.*, 2003, Figures 13 and 14] (hereinafter referred to as Paper 1))!

[3] Excellent reviews and summaries of previous work exist in the literature (e.g., Paper 1), and thus comprehen-

0148-0227/03/2003JE002057$09.00

sive duplication here is not warranted. For dust, a thorough discussion may be found in the combination of several key works [e.g., *Clancy and Lee*, 1991; *Murphy et al.*, 1993; *Clancy et al.*, 1995; *Pollack et al.*, 1995; *Ockert-Bell et al.*, 1997; *Tomasko et al.*, 1999, and references therein], while work on water ice is somewhat less voluminous [e.g., *Pearl et al.*, 2001; *Glenar et al.*, 2003, and references therein]. For the purposes of our work, it is sufficient to briefly mention the results relevant to particle size and variations thereof:

[4] 1. For dust, the most recent (i.e., 1995-present) work is consistent in deriving an average size (r_{eff}) of 1.5–1.7 μm, with the most precise retrievals coming from Pathfinder data [*Tomasko et al.*, 1999; *Smith and Lemmon*, 1999]. However, the agreement between the published Viking [*Pollack et al.*, 1995] and the Pathfinder [*Tomasko et al.*, 1999] retrievals is interpreted by some as an indication that the size has remained constant between the two epochs [e.g., *Tomasko et al.*, 1999; *Smith and Lemmon*, 1999]. Although the earlier Mariner 9 dust storm retrievals of much smaller and larger sizes [*Pang et al.*, 1976; *Toon et al.*, 1977] are considered problematic due to model approximations and assumptions [see *Clancy et al.*, 1995], the similarity of the Viking and Pathfinder retrievals represents only three spatial locations with limited temporal coverage. Clearly, more work can be done.

[5] 2. For water ice, the most direct measurement of size in the published literature is the Mariner 9 IRIS determination of $r_{eff} = 2$ μm [*Curran et al.*, 1973]. Although the large (regional-size) field of view may potentially include different cloud types (and sizes), the dominant cloud observed in this work is tentatively identified as a discrete, orographic cloud of the type commonly reported during the Mariner 9 and Viking epochs [*Smith and Smith*, 1972; *French et al.*, 1981]. Analysis of similar cloud structures, but using more indirect methods (e.g., solar illumination versus thermal emission of IRIS data) provides similar numbers (see section 7.1). However, the seasonal phenomenon often referred to as the Aphelion Cloud Belt (ACB) was not recognized prior to the mid-1990's [*Clancy et al.*, 1996]. The ACB, distinctly different from cloud structures previously identified, is now known to have been present during the Viking epoch through a recent reanalysis of Viking IRTM data [*Tamppari et al.*, 2000]. Preliminary estimates of particle size in the ACB using Thermal Emission Spectrometer (TES) observations have been previously reported by us to be in the 3–4 μm range [*Wolff et al.*, 2001; *Clancy et al.*, 2001]. This distinct dichotomy in particle size between the two types of clouds is found by *Glenar et al.* [2003] to be consistent with their analysis of near-IR spectra obtained during the aphelion season of 1999. Nevertheless, additional work in further quantifying the spatial and seasonal variations of water ice particle sizes is certainly needed.

[6] There is a requisite need for improvement in the current understanding of aerosol particle sizes and composition, particularly with respect to spatial and temporal variations (or lack thereof). An ideal data set with which to address such issues would possess comprehensive geographic and seasonal coverage, as well as a wavelength range containing spectral features unique to each aerosol component. Fortunately, with the arrival of TES on-board the Mars Global Surveyor (MGS) in 1997 and its nearly continuous operation through the present, such a data set now exists.

[7] The subject of the work presented here is the retrieval of aerosol properties from the MGS/TES IR spectroscopic data set. In combination with the TES solar band EPF analysis of Paper 1, it provides the most comprehensive and diagnostic study of Mars aerosols to date. While the primary goal of this IR spectral analysis is the characterization of aerosol particle sizes, accurate inversion of the TES data requires knowledge or simultaneous retrieval of several other important parameters. Consequently, significant detail is provided in terms of the algorithms employed, input parameters chosen, and precision of the results. We begin with a quick discussion of the conventions and nomenclature to be employed. Section 3 contains a brief description of the data to be used. Numerical details and theoretical particle size sensitivity are covered in sections 4 and 5, respectively. Next, we present the results of both "interactive" and automated retrievals. The "interactive" effort (section 6.1), which contains a total of 54 samples, is a survey from the point of view of both spatial and temporal sampling as well from that of "automation" algorithm development testing. Also presented in this section is the "effective uncertainty" for each retrieved parameter. The automated analysis effort (section 6.2) focuses on several regions of interest with temporal coverage that brackets the 2001 global dust storm. Finally, in section 7, our results are discussed in the context of Paper 1 and previous work, and their relevance to other areas of active interest to the Martian atmospheric research community.

2. Conventions

[8] Despite the existence of international standards and formal definitions, issues of units and nomenclature conventions remain a center of debate and discussion. For the convenience of the reader, we simply clarify a few of the conventions employed here.

[9] • Wavenumber versus wavelength. We will generally specify spectral locations "blueward" of 5 μm (2000 cm^{-1}) by wavelength, and "redward" by wavenumber. Such an approach approximates the observational convention of splitting the thermal IR and near-IR regions. It also avoids the effective ambiguity which inevitably results when referring to 0.7 μm as 14,285 cm^{-1}.

[10] • Optical depth and wavenumber. Unless specified, the use of the term "optical depth" (or its shorthand notation, τ) refers to that at either 1075 cm^{-1} (9.30 μm) or 825 cm^{-1} (12.1 μm) for dust or water ice aerosols, respectively.

[11] • The terms "dielectric function," "indices of refraction," and "optical constants" are used interchangeably throughout this document. Of course, the quantities in question are not constant in any useful sense, nor are the dielectric function (ϵ) and the complex index of refraction ($m = n + ik$) mathematically equivalent: i.e., $\epsilon = m^2$.

3. Data

[12] The TES IR spectral data examined in our interactive analyses (section 6.1) are taken from the populations of so-called "emission phase function" (EPF) sequences. Details

of this type of observation are given in Paper 1 (and references therein). In essence, a specific location on the surface is observed at various emission angles as the spacecraft passes over it. The sampling scheme of these data is such that one can, in principle, obtain additional leverage on both surface and atmospheric properties relative to that from nadir data. However, the combination of pointing drift [e.g., *Bandfield and Smith*, 2003] and nonuniform surface emissivity (section 4.6) provide sufficient motivation to confine our thermal IR analyses to the nadir observations. Angular information obtained from TES EPF sequences is employed in the companion TES solar band analysis (Paper 1). The more focused dust storm results of section 6.2 are not restricted to EPF sequences. Although all data are taken from "daytime" observations, analysis is done purely from the perspective of thermal emission by the surface and atmosphere. The "thermal" nature of the problem can be clearly seen using the solar irradiance compilation of *Wehrli* [1985, 1986]. Adjusting to a solar distance of 1.4 AU, one finds the ratio of incident (solar) to emitted irradiance at the surface Mars (assuming an emissivity of one) to be 1.0% (1.5%) at 1250 cm^{-1} for a temperature of 300 K (250 K); dropping by ~30–50% at 1000 cm^{-1}.

[13] A description of the TES instrument and its calibration characteristics may be found in several recent publications; the most comprehensive of which is the report of *Christensen et al.* [2001], where a very complete description of TES and its data products are given. For our purposes, it is sufficient to indicate that our spectra are a co-addition of all 6 essentially identical, but spatially offset, detectors for each integration (i.e., ICK). In addition, anywhere from 3–6 sequential ICKs (integrations) are also co-added to produce the modeled spectra. The error bars (σ_{data}) shown in the various plots in this paper are calculated using the Noise Equivalent Radiance values (for a single detector, 2.5×10^{-8} W cm^{-2} sr^{-1} cm^{-1} from 300 cm^{-1} to 1400 cm^{-1}; 6×10^{-8} W cm^{-2} sr^{-1} cm^{-1} at 250 cm^{-1}; 4×10^{-8} W cm^{-2} sr^{-1} cm^{-1} at 1450 cm^{-1}; linear interpolation used for 250–300 cm^{-1} and 1450–1600 $cm-^{1}$ ranges) added in quadrature with a background radiance uncertainty (1×10^{-8} W cm^{-2} sr^{-1} cm^{-1}). Co-addition is handled under the assumption of Poisson statistics for the noise term. However, the amplitude of the formal error is multiplied by two (i.e., increased 100%) in an attempt to allow for the effects of additional systematic, yet poorly constrained, errors in the data.

4. Modeling Details

4.1. IR Radiative Transfer

[14] Our model-data comparisons employ a modified version of doubling-adding radiative transfer code described by *Clancy et al.* [1995], which itself was adapted by Clancy et al. from the terrestrial atmospheric modeling code of *Gladstone et al.* [1984]. Our primary modifications include the option to include molecular opacity via a correlated-k algorithm [e.g., *Lacis and Oinas*, 1991], as well as the ability to handle arbitrary surface emissivity spectra and aerosol dielectric functions. Following *Clancy et al.* [1995], we specify the atmospheric vertical structure using a resolution of 2 km for altitudes of 0–20 km, and 5 km over 20–60 km. This choice of vertical spacing was motivated primarily by the need to adequate resolve the aphelion cloud belt "bottom" heights (i.e., water vapor saturation points) with respect to changes in model radiances without unnecessarily increasing the computational intensity of the model. In addition, as mentioned previously, we do not consider the contribution of incident solar radiation to the TES data.

4.2. Vertical Structure

[15] The temperature (vertical) profiles are constructed from the TES nadir surface pressure and atmospheric temperature retrieval products [*Conrath et al.*, 2000]. The interested reader is referred to Conrath et al. for details and caveats on these TES products; we adopt them "as is" (we only use data with a "good" quality flag). The connection of pressure to altitude is specified by the equation of hydrostatic equilibrium. Temperature values between the surface and the lowest altitude for which a temperature was retrieved by the TES team algorithm (typically ~1–2 km) are calculated using linear extrapolation. Atmospheric temperatures above the 0.1 mbar pressure level (~40 km) are extrapolated to the 0.002 mbar using a logarithmic pressure mesh. A minimum temperature of 140 K is set within these top layers of radiative transfer integration. The altitude of the surface for a TES footprint is taken from the Mars Orbiter Laser Altimeter topography map with 1° resolution [e.g., *Smith et al.*, 2001, and references therein].

[16] The minimal amount of aerosol vertical distribution information derivable from TES nadir observations leads to an assumption that particle sizes are constant as a function of altitude. We also implement a set of simple, but physically plausible algorithms for the aerosol mixing ratio profile. Water ice is also assigned a constant mixing ratio, but the lower altitude boundary is specified by water vapor saturation conditions [*Clancy et al.*, 1996]. The constant ice mixing ratio is extended to the top of the model atmosphere (i.e., 60 km). Experimentation with more confined clouds (and dust), such as confined to altitudes <20–25 km, do not provide measurable differences in either the particle sizes or total column, even at aphelion were water vapor saturation altitudes are quite low (5–10 km [e.g., *Clancy et al.*, 1996]). For dust, we assume a uniform mixing through the atmosphere. Here, retrieval errors associated with uncertain dust vertical distributions are also small. For particle sizes, numerical experimentation with very nonuniform mixing (including up to a 2000% enhancement of the mixing ratio in the bottom 1 km of the atmosphere) produces scatter within the size retrieval uncertainties found for the uniform case. In terms of dust optical depth, the largest departures from uniform mixing are most likely to occur during the low dust loading periods [e.g., *Conrath*, 1975; *Toigo and Richardson*, 2000]. *Toigo and Richardson* [2000] estimate an upper limit of 10% uncertainty between uniform mixing and more "plausible" distributions which might be effectively capped at the 6–10 km height. However, their analyses were performed on Viking broad-band IR observations; performing similar tests with the TES spectra from the same seasons, we find differences to be below 5%. For dusty observations, "physically plausible" distributions would be expected to much closer to uniform mixing. Using

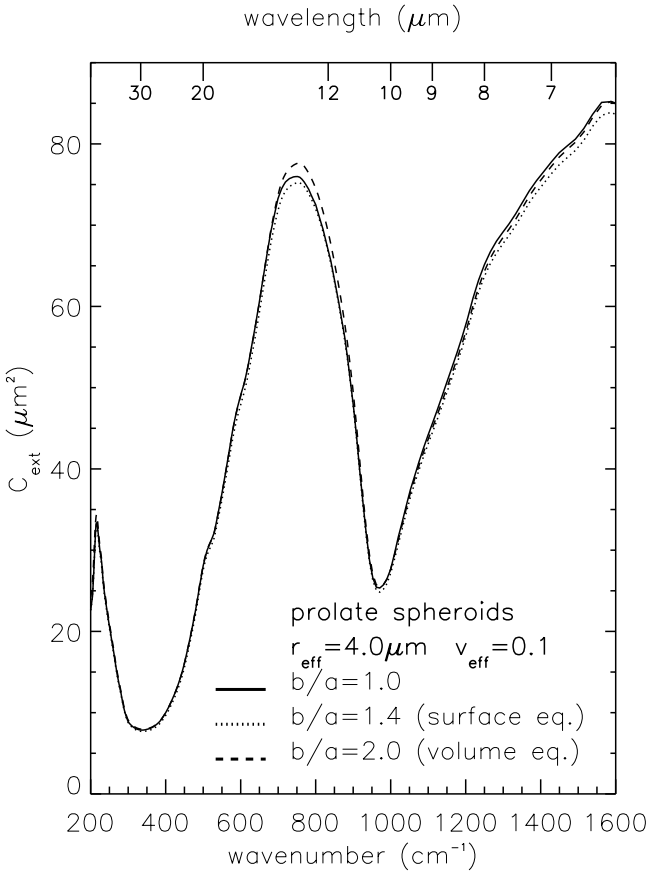

Figure 1. The extinction cross section for a sphere composed of water ice is compared to that for two randomly oriented prolate spheroids. Each spheroid has an axial ratio indicated by the b/a value. The size distribution is specified with a modified-gamma size distribution having the indicated moments, r_{eff} and v_{eff} (as defined by *Hansen and Travis* [1974]). The size of the spheroids depends on the particular "equivalent-sphere" convention. Relative to the sphere, the b/a = 1.4 spheroid has the same surface area, while the b/a = 2.0 spheroid has the same volume.

the vertical distribution of *Conrath* [1975] for the 1971 dust storm (i.e., Conrath's $\nu \sim 0.01$), we find differences of, at most, a few percent when compared to uniform mixing.

4.3. Particle Cross Sections

[17] The largely absorbing nature of aerosols in the 200–1500 cm^{-1} range suggests the utility of inverting the observed radiances using a purely absorbing atmosphere. Although this is reasonable if extreme computational efficiency is desired, it does underestimate the total aerosol column. Although we will address this in section 7.2, *Smith et al.* [2000a, 2000b] estimate the uncertainty with the neglect of scattering to be ~20–25%. However, our interest is in actual particle properties, and so a full multiple-scattering treatment is required. Fortunately, the radiative transfer problem in the TES spectral regime is typically dominated by forward- and near-forward scattering effects. As has been pointed out previously [cf. *Bohren and Huffman*, 1983; *West*, 1991], the diffraction peak and the forward-scattering quantities (i.e., extinction cross section, single scattering albedo, etc.) are only weakly dependent on particle shape. This is illustrated in Figure 1 where the extinction cross section (C_{ext}) of a sphere is compared with those of two randomly oriented prolate spheroid distributions. The particles are composed of water ice and present sizes near the maximum values retrieved during the course of this investigation. Of course, one might intuitively object that for smaller particles and wavenumbers (e.g., smaller size parameters), the "shape" of a phase function may not be clearly dominated by the diffraction lobe. While one could certainly quibble about the definition of "near-forward" and the width of diffraction lobe, the fact remain that for size parameters ($2\pi r/\lambda$) $\lesssim 2-3$, the difference in phase function between spherical and moderately oblate/prolate (e.g., axial ratios $\lesssim 2$ or $\gtrsim 0.5$) particles is at or below the level of 5–10% for scattering angles less than 90°. [e.g., *Mishchenko et al.*, 1996]. In addition, these particles also have smaller single scattering albedos and thus further minimize the differences between spherical and nonspherical shapes. Consequently, the case shown in Figure 1 represents a "worst-case" scenario: smaller sizes have better agreement, as do dust aerosols in general (due to their lower single scattering albedo). The errors introduced into modeled extinction cross sections under the assumption of spherical aerosols are a few percent at most across the TES spectral range.

[18] The aerosol cross sections are computed using standard Mie theory [e.g., *Bohren and Huffman*, 1983] as implemented in the publicly available code, DMiLay ftp://climate.gsfc.nasa.gov/pub/wiscombe/Single_Scatt/Coated_Sphere/). The scattering phase function is sampled at 1° intervals.

4.4. Dielectric Function

[19] We consider only two basic aerosol materials: water ice and "dust." The dielectric function for the former is taken directly from the work of *Warren* [1984] and collaborators (see also ftp://climate.gsfc.nasa.gov/pub/wiscombe/Refrac_Index/ICE/). For dust, we adopt a dielectric function that is a synthesis of recent work in the optical and thermal IR [*Clancy et al.*, 1995, and references therein]; *Snook*, 1999; *Tomasko et al.*, 1999; [*Snook et al.*, 2000; G. Hansen, personal communication, 2001] with modifications made during the course of our investigation.

[20] Figures 2 and 3 compare the imaginary and real parts of our final complex indices of refraction with those from which portions were taken for our initial set optical constants. The process employed in deriving the adopted function is an iterative one. We construct a range of imaginary index (k) values and then compute the associated real (n) indices using a subtractive Kramers-Kronig (SKK) algorithm, kindly supplied by Kelly Snook [*Snook*, 1999; see also *Warren*, 1984]. The SKK is variation of the classical Kramers-Kronig algorithm that allows one to effectively reduce the range of integration. In practice, one is able to derive n values for the desired wavelength range without including k values for regions well beyond by range boundaries (as would need to be done for classical KK). The fixed-point value of n needed for the SKK calculations is typically taken to be 1.5 for a wavelength of 0.5 μm (20,000 cm^{-1}). Using fixed-points at other spectral locations (e.g., from thermal IR laboratory measurements in the 1500–

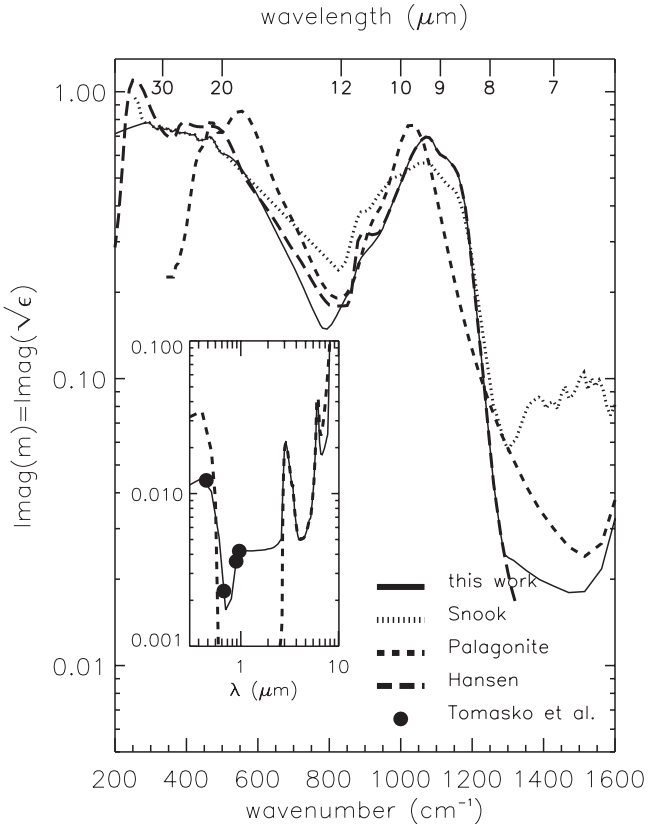

Figure 2. Comparison of the imaginary part (k) of the adopted complex indices of refraction ($m = n + ik = \sqrt{\varepsilon}$) to those of the components used as initial values. The "palagonite" material is that published by *Clancy et al.* [1995]. See text for further details.

2000 cm^{-1}) does not significantly alter the derived n. Next, in order to assess the "validity" of the new dielectric function, we conduct model-data comparisons for a set of TES observations of low-to-moderate dust optical depths (τ_{dust} = 0.1–0.7), for which other analyses have generally indicated that there is very little change in particle sizes [*Bandfield et al.*, 2000; *Smith et al.*, 2000a, 2000b]. The spectral regions which demonstrate a poor agreement have the associated k "updated." The process naturally repeats itself until the model-data comparisons provide a fit within the observational errors and estimated model uncertainties.

[21] Our initial set of k values is taken from the palagonite material given by *Clancy et al.* [1995] (the thermal IR values were originally published by *Roush et al.* [1991]). The 700–1430 cm^{-1} (7–14.3 μm) and 285–500 cm^{-1} (20–35 μm) regions are replaced with a smoothed (3 point boxcar filter) set of indices from *Snook* [1999], *Snook et al.* [2000], and K. Snook (personal communication, 2001), with a cubic spline interpolation used for the 500–700 cm^{-1} range. "Redward" of 285 cm^{-1} (35 μm), we assume a power-law extrapolation ($k \propto \lambda^{-0.25}$), as has been done for similar materials in the IR in the absence of laboratory data [e.g., *Pollack et al.*, 1994]. The exact value of the power-law exponent is not particularly well-constrained by the TES data considered. That is to say, an exponent of −0.5 can be adopted without appreciably changing the quality of the fits, particularly given the much lower quality of the data in this spectral region. However, model-data comparisons did show deficiencies in the region of the 1075 cm^{-1} silicate absorption feature, including the adjacent "continuum." Modifications to the initial set of k's include the use of imaginary indices for 7.7–10.5 μm from an analysis of Mariner 9 observations (G. Hansen, personal communication, 2001). We enforce a "smooth" transition between the different k sets by essentially interpolating linearly between the 1300–1667 cm^{-1} (6–7.7 μm) and 850–950 cm^{-1} (10.5–11.7 μm) intervals. Finally, due to our interest in the TES visible bolometer data, the 0.3–2.9 μm (3450–33,333 cm^{-1}) k values are adjusted to agree with those from the "Size 1" case of *Tomasko et al.* [1999].

4.5. Nadir Surface Emissivity

[22] The surface of Mars has a surface emissivity which is very rarely, if ever, equal to unity over the TES spectral region [e.g., *Bandfield*, 2002]. Consequently, efforts to retrieve atmospheric particle properties may be significantly biased without an accurate representation of this important surface property. We use a nadir surface emissivity map kindly supplied to us by J. Bandfield, based on his work cited above. The data set used in the map product was taken in 10 cm^{-1} sampling mode and avoided the use of any observations containing significant amounts of dust and water ice. The data were corrected for dust aerosol and

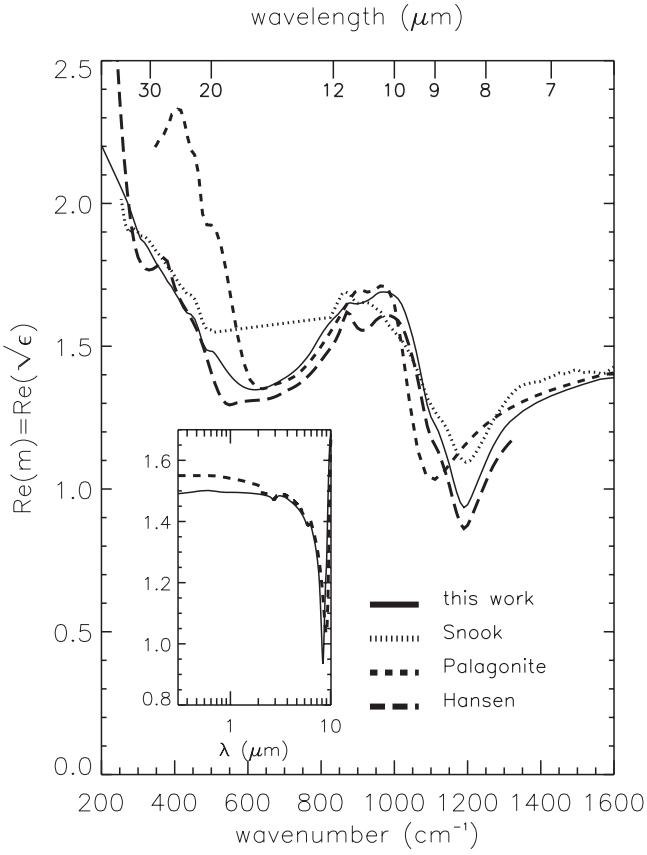

Figure 3. As for Figure 2, but for the real part (n) of the complex indices of refraction. *Tomasko et al.* [1999] assumed a constant value of n = 1.5.

co-added spatially into 1° × 1° bins. The spectra are clipped spectrally below 250 cm^{-1} (poor signal-to-noise), above 1300 cm^{-1} (problems with atmospheric correction, and to a lesser extent, poor signal-to-noise), and 510–820 cm^{-1} (main CO_2 feature). H_2O vapor and minor/isotopic CO_2 bands remain in the maps, though the former contribution is minimized due to the temporal and spatial variability of H_2O vapor abundances [e.g., *Smith*, 2002].

[23] For the case of clearly noisy emissivity spectra, we apply a three-point (spectral) boxcar filter. While most of our analysis is confined to the spectral regions covered by the maps, the inclusion of the CO_2 band is handled by quadratic interpolation across that region.

4.6. Directional Surface Emissivity

[24] The concept that a particulate surface should emit radiation isotropically (e.g., like a Lambert surface) is only valid, theoretically at least, for an emissivity of unity [*Hapke*, 1993, 1996]. Recent work using TES EPF observations indicates that one might be able to find regions on the surface where the so-called "directional emissivity" effects are minimized [*Pitman et al.*, 2001; *Bandfield and Smith*, 2003]. However, in light of the current lack of validated nonnadir surface emissivity maps or models, we focus on the analysis of the nadir pointings.

4.7. Automated Least Squares Minimization

[25] For our automated retrievals, we employ the IDL-based MPFIT routines developed by Craig Markwardt http://cow.physics.wisc.edu/~craigm/idl/idl.html). Essentially, MPFIT is based on the well-known and tested MINPACK-1 FORTRAN minimization library [*Moré et al.*, 1984]. In fact, the code is often a direct translation from the original FORTRAN routines. Our "driver" implementation makes multiple calls to MPFIT in order to provide additional control during the iteration procedure. More specifically, we iterate first on surface temperate and optical depth, leaving r_{eff} fixed (and v_{eff}, of course). A second set of iterations follows, allowing r_{eff} to vary. Poor fits are subjected to additional calls to the MPFIT library after perturbing the initial guess for r_{eff} from the previous step. The figure of merit for convergence is the traditional χ^2 statistic weighted by the data variances: i.e., $\chi^2 = \Sigma\ ((data - model)/\sigma_{data})^2$.

5. Theoretical Retrieval Sensitivity

[26] In principle, the TES spectral range is ideally suited to identify the presence of water ice and dust aerosols as well as to retrieve the individual component optical depths and particle sizes. In practice, one must exercise some care in defining what is being "retrieved" and in understanding the limitations set by observational (and systematic) error. In this section, we define the particle size that we measured in our model-data comparisons (section 6) as well as demonstrating the sensitivity of idealized TES spectra to particle size. We will address systematic effects in section 6.

[27] Since one does not expect particles in the Martian atmosphere to be monodisperse, the concept of particle size must be defined with respect to a size distribution of particles. *Hansen and Travis* [1974] find that characterizing size using moments of the distribution is an excellent approach. In fact, they demonstrate that the exact form of the size distribution is not generally critical as long as a sufficient number of moments are used in setting the parameters of the distribution. Typically, only the first two moments are needed. As defined by *Hansen and Travis* [1974], r_{eff} and v_{eff} are the mean and the dimensionless variance of the size distribution as weighted by the geometrical cross section of the particles. For historical, though admittedly somewhat arbitrary, reasons we adopt the modified gamma distribution [*Deirmidjian*, 1964] for the work presented here:

$$\frac{dn(r)}{dr} = C\ r^a\ exp(-br^c)$$

where the normalization constant (C) is $b^{(a+1)/c}c/\Gamma((a+1)/c)$, Γ is the classical "gamma function," r is the particle (equivalent sphere) radius, and (a, b, c) are constants which may be adjusted to provide the desired r_{eff} and v_{eff}.

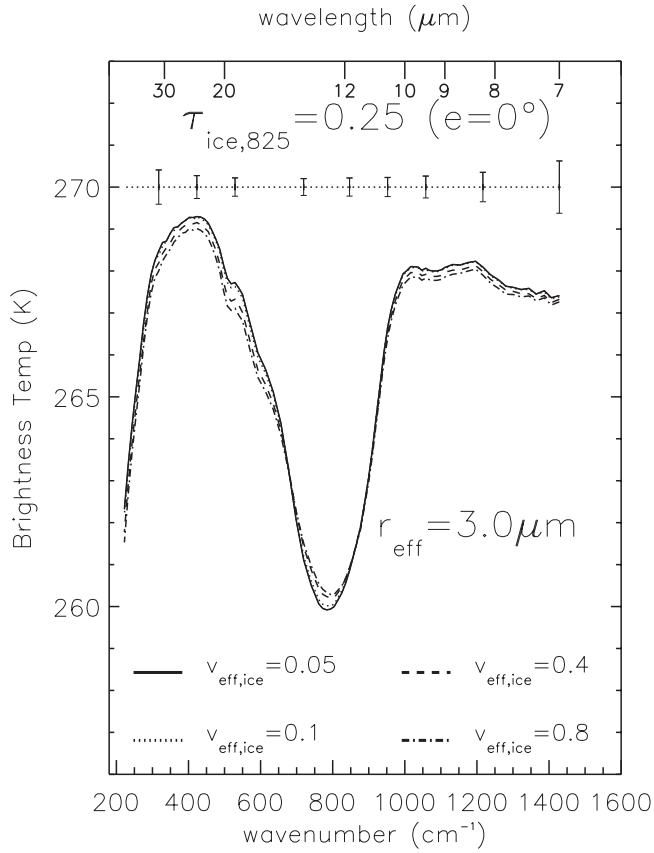

Figure 4. Sensitivity of a theoretical nadir TES spectrum to differences in v_{eff} for water ice particles. The models shown here are calculated using a unit surface emissivity at all wavenumbers, r_{eff} = 3 μm, representative errors for a single TES detector as describe in section 3, and atmospheric temperature data representative of conditions near the equator during mid-to-late northern spring season (ock 8960, icks 1962–1966, L_S = 67°) with a surface temperature of 270 K. CO_2 absorption has been omitted for clarity.

5.1. Water Ice

[28] TES spectra are not particularly sensitive to the value of v_{eff} in water ice particle size distributions. This is demonstrated in Figures 4 and 5, where model spectra of

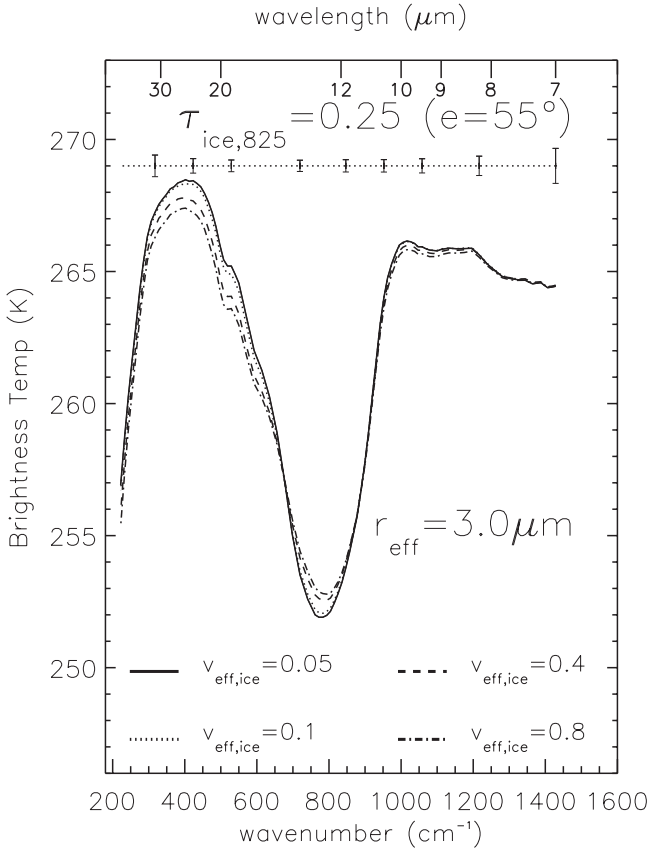

Figure 5. Sensitivity of a theoretical off-nadir TES spectrum to differences in v_{eff} for water ice particles for constant τ_{ice}. As for Figure 4, but with an emission angle of 55°. Surface emission is assumed to be constant as a function of emission angle (i.e., Lambertian).

ice aerosols are presented with various values of v_{eff} for a constant r_{eff}. These model calculations employ the idealized case of a unit surface emissivity, but incorporate vertical temperature distributions and surface temperatures fairly representative of Martian conditions (see figure captions for details). Even for the most optimal off-nadir case, one could only hope to differentiate between very narrow versus very broad distributions. The Mariner 9 IRIS analyses of *Curran et al.* [1973] use a fairly narrow distribution, $v_{eff} = 0.032$. Guided by numerical experimentation, we adopt a more moderate $v_{eff} = 0.1$. However, we emphasize that both values ($v_{eff} = 0.1$ and 0.032) produce essentially the same retrievals from TES spectra.

[29] Fortunately, as shown in Figures 6 and 7, TES IR spectra present much greater sensitivity to r_{eff} versus v_{eff} (τ_{ice} is held constant). Even when restricted to nadir geometry (i.e., e = 0°), but with sufficient opacity, one can clearly discriminate $r_{eff} = 1-2$ μm particles from values of 3 or 4 μm. The reduced discrimination among smaller particle sizes reflects the reduced importance of the particle size (relative to wavelength) in scattering processes at small size parameters ($2\pi r_{eff}/\lambda$).

5.2. Dust

[30] Figure 8 indicates that dust aerosols are subject to increased sensitivity for v_{eff} relative to that for water ice (due in part to the increased optical depths for dust column). Nevertheless, it is still insufficient to provide accurate retrieval even for e = 55° (not shown). Specific details of the calculations are included in the figure caption. Guided by previous work, we adopt a more typical v_{eff} value between the lower limit of 0.2 set by *Tomasko et al.* [1999] and the broadest distribution considered by, e.g., *Clancy et al.* [1995]: $v_{eff} = 0.4$. Such a value is generally consisting with previous studies, includ-

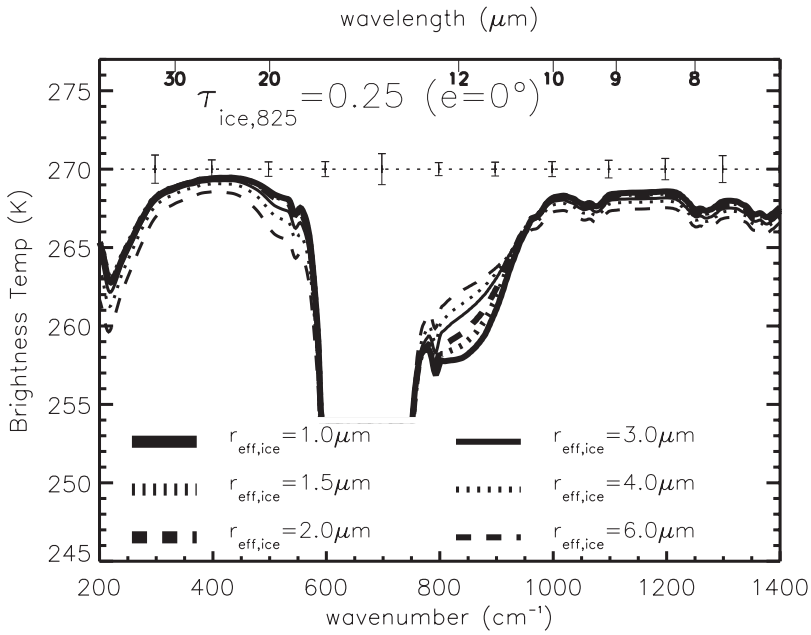

Figure 6. Sensitivity of a theoretical nadir TES spectrum to differences in r_{eff} for water ice particles (for constant τ_{ice}). As for Figure 4, but now r_{eff} is varied while the second moment is held constant ($v_{eff} = 0.1$).

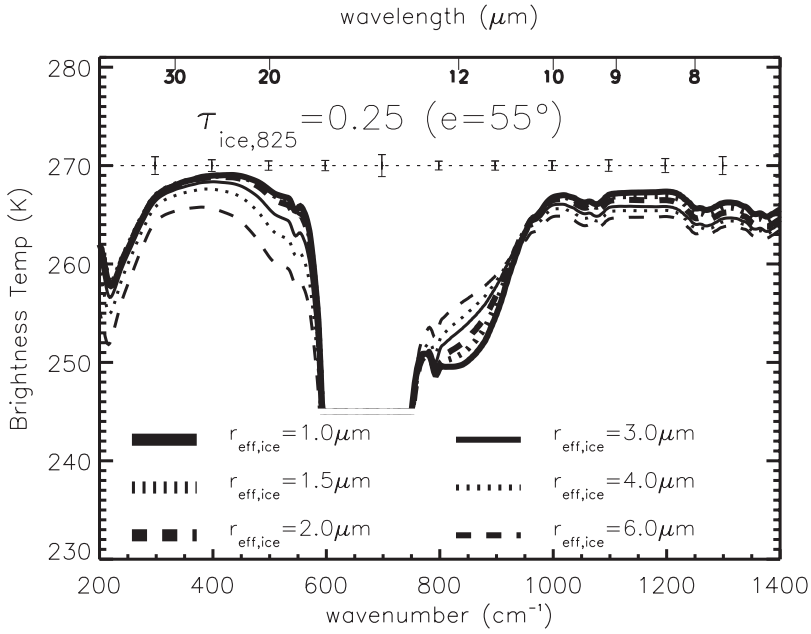

Figure 7. Sensitivity of a theoretical off-nadir TES spectrum to differences in r_{eff} for water ice particles (for constant τ_{ice}). As for Figure 6, but with an emission angle of 55°. Surface emission is assumed to be constant as a function of emission angle.

ing the *Clancy et al.* [1995] dust size solution for a wavelength dependent surface emissivity (now shown to be the case from TES analysis). Figure 9 presents the dependence of the model radiance to r_{eff}. As with ice particles, the reduction in contrast for the 1–2 μm region (as compared to 2–3 μm) is a natural consequence of electromagnetic scattering behavior. However, the canonically larger dust optical depths, relative to those typically

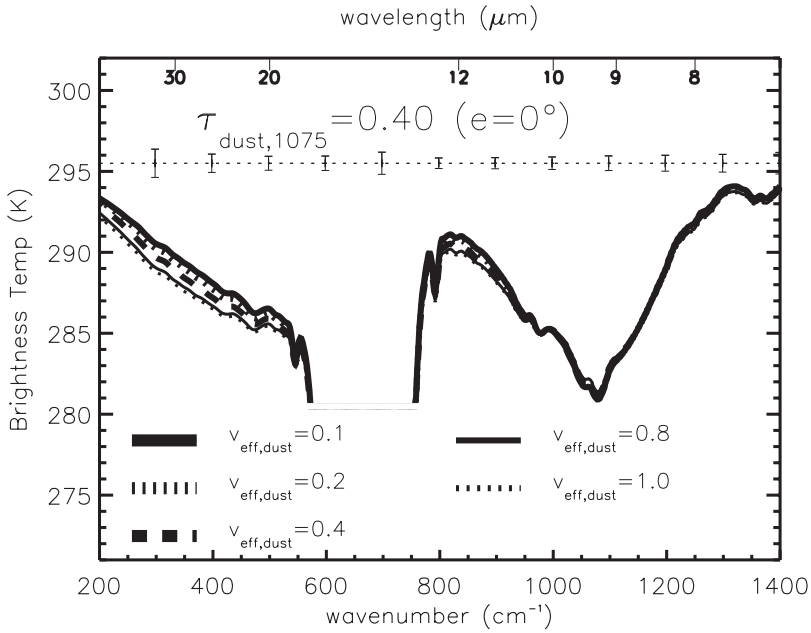

Figure 8. Sensitivity of a theoretical nadir TES spectrum to differences in v_{eff} for dust particles (constant τ_{dust}). The models shown here are calculated using a unit surface emissivity at all wavenumbers, r_{eff} = 1.5 μm, representative errors for a single TES detector as describe in section 3, and atmospheric temperature data representative of conditions in the equatorial and mid-latitudes during early southern summer (ock 4242, icks 1629–1631, L_S = 218°) with a surface temperature of 296 K. CO_2 absorption has been omitted for clarity.

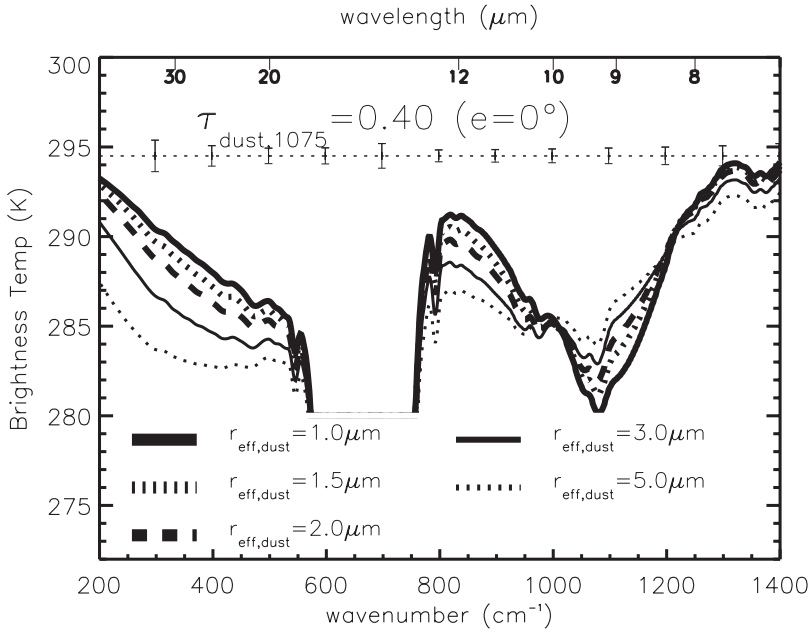

Figure 9. Sensitivity of a theoretical nadir TES spectrum to differences in r_{eff} for dust particles (constant τ_{dust}). As for Figure 8, but now r_{eff} is varied while the second moment is held constant ($v_{eff} = 0.4$).

found for water ice, can adequately compensate for the weak size-dependence.

6. Results

[31] Our analysis procedure derives five parameters: two aerosol optical depths (τ_{dust}, τ_{ice}), two sizes ($r_{eff,dust}$, $r_{eff,ice}$), and surface temperature (T_{surf}). This modest number of variables, when combined with the modest formal errors associated with the typical TES spectrum (particularly when using co-added data), suggests the viability of a completely automated retrieval algorithm. However, systematic errors in both the observations and adopted model parameters (e.g., surface emissivity, aerosol dielectric properties) can significantly increase retrieval uncertainties beyond simple measurement error constraints. In essence, ''geophysical'' variances not represented in the models of section 5, contribute spectrally correlated errors or ''local minima'' in χ^2 space. This is particularly problematic for the case of water ice aerosols where much of the main absorption feature is masked by the main CO_2 band at 667 cm^{-1}. As a result, we apply a combination of interactive and automated analyses. Application of the former technique provides a survey of aerosol properties (spatial and temporal) in addition to set of results against which to test automated algorithms and EPF solar-IR comparisons (Paper 1). The latter allows us to present two limited, but focused, analyses of particle properties associated with the 2001A global dust storm using hundreds, rather than tens, of model fits.

6.1. Interactive Survey Analyses and Retrieval Uncertainties

[32] The range of observations chosen for our ''interactive'' effort is driven by a desire to sample the temporal and spatial variations of aerosol properties associated with the three general types identified in Paper 1: dust, water ice Type 1, and water ice Type 2. The results of these retrievals are given in Tables 1–3. Unless otherwise noted, the classification of the individual spectra into the three categories is based solely on the shape of the phase functions used in analyses of the visible bolometer EPF sequences presented in Paper 1. The individual observations are chosen by combining queries of the TES team optical depth retrievals with visual inspection of candidate spectra. Of course, this task remains manageable due to our restriction to daytime EPF sequences.

6.1.1. Surface Temperature Uncertainty

[33] The formal precision (i.e., approximating the covariance matrix), $\sigma_{prec.}$, associated with the surface temperature values is $\lesssim$0.1 K for the range of optical depths and surface temperatures studied (including those from the fully automated retrievals presented below). The accuracy in T_{surf} is directly dependent on the errors in the surface emissivity spectra. *Bandfield* [2002] provides an upper bound of 0.003 on the emissivity errors. Even the allowance for an error that is five times greater (i.e., 0.015) provides an accuracy in T_{surf} to better than 0.5 K for a 230 K surface. Contributions due to errors in aerosol properties are generally minimized by focusing on the ''transparency'' region (i.e., 1200–1300 cm^{-1}) where opacity is low, but surface emissivity is at a maximum. Combining the above accuracy and precision algorithms yields an ''effective uncertainty,'' $\sigma_{T,eff}$, of 0.2–0.3 for $T_{surf} \gtrsim 250$ K. However, for simplicity, we adopt the conservative estimate of $\sigma_{T,eff} = 0.5$ K.

6.1.2. Optical Depth Uncertainty

[34] For optical depth, the situation is more complicated as it is a more sensitive function of absolute aerosol loading, surface temperature, and adopted optical constants/surface emissivity. On the other hand, estimation of the formal precision is simplified by the weak dependence on particle size. For our adopted vertical distribution $\sigma_{prec.}$ is typically in the 2–5% range, though it can reach 10–15% for high

Table 1. Modeled TES Data: "Dust"

						TES Team				This Work					
ock	ick	L_S, °	emis, °	long, °	lat, °	τ_d	τ_i	T_{surf}, K	P_{surf}, mb	τ_d	τ_i	T_{surf}, K	$r_{eff,d}$, μm	$r_{eff,i}$, μm	Comments[a]
3631	1803	188.2	0.6	173.4	5.9	0.16	0.04	280	6.9	0.21	0.04	282	1.8	1.6	
4242	1630	218.1	4.5	21.7	−11.8	0.25	− 0.01	294	6.8	0.39	0.00	296	1.6	...	
4279	1779	219.9	0.6	2.7	3.4	0.21	0.01	284	6.6	0.32	0.02	285	1.6	1.6	
4353	2079	223.7	0.6	325.3	34.0	0.19	0.08	237	6.4	0.25	0.04	239	1.5	1.6	
4457	2774	229.0	0.6	53.6	−30.1	0.46	− 0.02	290	5.4	0.68	0.00	292	1.9	...	
4545	1240	233.5	4.0	49.0	−51.6	0.49	0.00	273	7.8	0.72	0.00	275	1.6	...	
4712	3029	242.2	0.6	159.6	18.7	0.51	0.01	256	8.8	0.71	0.02	258	1.5	1.6	
5404	1306	277.9	0.6	159.4	−44.9	0.12	0.01	300	4.8	0.16	0.02	300	1.5	1.6	
5451	1161	280.2	0.6	61.4	−59.7	0.11	0.01	292	5.7	0.13	0.00	293	1.5	...	
6188	1893	316.3	0.6	288.2	9.4	0.09	0.02	295	4.9	0.13	0.00	295	1.5	...	
6392	1893	325.7	0.6	8.1	15.0	0.23	0.02	272	6.8	0.34	0.02	273	1.6	...	
7847	2340	25.9	0.6	264.8	60.1	0.15	0.04	239	8.5	0.19	0.05	240	1.5	1.6	
8241	2079	40.5	0.6	18.7	33.6	0.20	0.04	270	8.7	0.25	0.04	272	1.5	1.6	
8381	1452	45.7	0.6	58.1	−29.9	0.07	0.04	244	5.1	0.11	0.03	244	1.5	1.6	
11841	2041	179.1	0.6	171.4	29.9	0.09	0.02	274	7.2	0.17	0.02	275	1.6	1.6	
11931	2041	183.2	0.6	230.4	29.9	0.14	0.01	272	7.6	0.23	0.01	273	1.7	1.6	
12021	2031	187.5	0.6	289.5	30.1	0.75	−0.01	245	5.1	0.94	0.04	247	1.4	1.6	1
12039	1374	188.3	0.6	75.8	−38.1	0.14	0.00	274	3.6	0.26	0.00	275	2.1	...	
12051	1452	188.9	0.6	60.9	−30.1	0.24	0.00	276	4.2	0.35	0.00	277	1.9	...	
12059	1520	189.2	0.6	291.1	−22.8	1.22	0.12	244	5.7	1.59	0.04	246	2.4	1.6	
12062	1814	189.4	0.6	21.1	6.8	0.47	− 0.01	273	6.6	0.66	0.00	274	1.8	...	
12148	1599	193.5	0.6	322.5	−14.8	1.23	0.01	266	4.0	1.68	0.00	269	2.0	...	
12157	2041	193.9	0.6	226.5	29.9	0.59	− 0.02	252	7.7	0.81	0.00	253	1.4	...	
12322	2041	201.9	0.6	274.5	30.2	1.12	0.11	231	7.4	1.46	0.07	232	1.7	1.6	2
12397	2041	205.6	0.6	263.6	30.2	1.00	− 0.03	231	8.1	1.79	0.00	234	1.6	...	
12412	2031	206.3	0.6	333.3	29.9	1.00	− 0.07	230	6.3	1.61	0.05	232	1.3	1.6	1,2
12463	1599	208.9	0.6	348.5	−14.9	2.01	− 0.07	253	5.1	2.49	0.00	257	1.7	...	2
12700	1452	220.7	0.6	297.3	−28.2	2.09	−0.03	250	7.3	2.45	0.03	253	1.7	1.6	2

[a]Comments: 1, v_{eff} = 0.2; 2, TES optical depths flagged as "questionable."

optical depths and lower surface temperatures (e.g., $T_{surf} \lesssim$ 240 K). However, these numbers do not appreciably change for other "plausible" vertical distributions (section 4.2). Systematic errors tend to dominate at low τ and subsequently set the level of accuracy. Simple numerical experiments which apply perturbations to the various input parameters provide useful estimates; typically one parameter at a time is perturbed and held fixed during subsequent iterations. For the dielectric functions, surface emissivity spectra, and vertical aerosol distributions employed here, the accuracy of τ is in the range of 0.03–0.04 for dust and 0.02–0.03 for water ice. Since we find that one of the two terms tends to dominate in most cases, we simply specify $\sigma_{\tau,eff}$ as $max(\sigma_{prec}, \sigma_{acc})$. For the tabulated τ, one may use $max(0.04, 0.1\ \tau_{dust})$ and $max(0.03, 0.1\tau_{ice})$ for dust and ice, respectively.

6.1.3. Particle Size Uncertainty

[35] Uncertainty in the retrieved particles sizes is distinctly different for dust and water ice. For a fixed v_{eff}, r_{eff} is varied by adjusting the b parameter of the modified gamma distribution. The covariance matrix approach finds that the uncertainty in b for dust particles is generally a few percent at most. However, for water ice aerosols, the uncertainty is larger: usually from 10% for the larger particles to 20% for the smaller ones. With a fixed effective variance of v_{eff} = 0.4 (dust), a 5% uncertainty translates to ±0.15 μm for

Table 2. Modeled TES Data: "Ice Type 1"

						TES Team				This Work					
ock	ick	L_S, °	emis, °	long, °	lat, °	τ_d	τ_i	T_{surf}, K	P_{surf}, mb	τ_d	τ_i	T_{surf}, K	$r_{eff,d}$, μm	$r_{eff,i}$, μm	Comments
1813	1831	112.1	0.6	327.6	−2.3	0.07	0.06	266	4.3	0.08	0.08	266	1.5	1.5	
2070	1597	121.9	0.6	123.9	−15.2	0.04	0.09	249	2.4	0.04	0.12	248	1.5	1.5	
2407	1683	135.1	0.6	53.5	−6.8	0.11	0.17	265	3.9	0.06	0.25	267	1.5	2.0	
2469	1977	137.6	0.6	32.6	23.5	0.07	0.04	282	6.9	0.12	0.04	283	1.5	1.5	
2515	1683	139.4	0.6	265.7	−6.3	0.09	0.12	271	4.2	0.05	0.11	271	1.5	1.5	
2610	1595	143.3	0.6	104.4	−15.1	0.02	0.05	257	2.5	0.05	0.09	258	1.5	1.6	
4353	2081	223.7	0.6	325.3	34.0	0.19	0.08	237	6.4	0.21	0.05	238	1.5	1.7	
7337	1452	6.0	0.6	51.7	−29.8	0.14	0.04	267	5.1	0.15	0.04	267	1.5	1.6	
7805	1452	24.3	0.6	128.4	−29.9	0.02	0.03	249	4.4	0.05	0.06	250	1.5	1.8	
8549	1520	51.7	0.6	188.9	−23.1	0.04	0.04	243	5.1	0.06	0.05	244	1.5	1.5	
8598	1599	53.5	0.6	152.9	−14.6	0.05	0.08	253	5.3	0.08	0.11	255	1.5	1.5	
8876	1929	63.5	0.6	196.7	18.6	0.07	0.07	265	7.1	0.04	0.10	266	1.5	2.0	
9162	1599	73.7	0.6	101.3	−14.8	0.03	0.08	242	2.8	0.02	0.10	242	1.5	1.5	
9437	1479	83.5	0.6	54.0	−27.4	0.02	0.04	237	5.1	0.05	0.06	237	1.5	1.5	
9818	1746	97.3	0.6	168.4	0.0	0.11	0.13	260	7.1	0.08	0.15	260	1.5	1.9	
9929	1599	101.3	0.6	105.2	-15.3	0.07	0.11	241	2.8	0.08	0.15	242	1.5	1.5	

Table 3. Modeled TES Data: "Ice Type 2"

						TES Team				This Work					
ock	ick	L_S,°	emis,°	long,°	lat,°	τ_d	τ_i	T_{surf}, K	P_{surf}, mb	τ_d	τ_i	T_{surf}, K	$r_{eff,d}$, μm	$r_{eff,i}$, μm	Comments[a]
1886	1831	114.9	0.6	259.9	14.6	0.11	0.14	265	6.7	0.09	0.23	268	1.5	3.2	
2038	1831	120.7	0.6	291.2	10.8	0.09	0.17	282	4.0	0.03	0.28	285	1.5	3.3	
2056	1831	121.4	0.6	86.1	6.9	0.15	0.27	263	4.4	0.06	0.39	265	1.5	3.0	
2345	1831	132.6	0.6	81.0	12.6	0.08	0.18	271	4.9	0.05	0.25	273	1.5	3.0	
2420	1830	135.6	0.6	37.2	0.6	0.15	0.32	268	4.6	0.03	0.52	272	1.5	3.2	1
2434	2125	136.2	0.6	112.9	38.7	0.13	0.40	267	2.6	0.03	0.54	270	1.5	1.8	1
2516	1830	139.5	0.6	296.3	8.7	0.08	0.12	285	3.9	0.06	0.18	287	1.5	3.2	
8155	1780	37.4	4.5	72.6	3.5	0.10	0.16	272	4.8	0.04	0.21	274	1.5	1.8	
8180	1893	38.3	0.6	69.8	15.1	0.13	0.11	274	5.7	0.11	0.19	276	1.5	3.0	
8900	1929	64.3	0.6	163.9	18.5	0.12	0.11	266	8.2	0.07	0.15	272	1.5	2.5	
8959	1814	66.4	0.6	51.7	7.0	0.09	0.15	259	5.9	0.06	0.23	262	1.5	3.0	
8960	1962	66.5	0.6	82.3	22.0	0.09	0.12	270	5.7	0.06	0.20	273	1.5	3.0	
8986	2190	67.4	0.6	110.4	45.1	0.12	0.25	262	3.6	0.03	0.34	264	1.5	2.5	1
9391	1746	81.9	0.6	180.5	0.0	0.09	0.12	260	7.0	0.10	0.21	263	1.5	3.1	
9699	1893	92.9	0.7	2.4	14.8	0.09	0.12	268	6.3	0.08	0.21	270	1.5	3.4	
10560	1746	125.1	0.6	181.3	0.1	0.10	0.12	267	6.2	0.10	0.17	268	1.5	3.0	
10649	1962	128.5	0.6	214.0	21.9	0.18	0.38	270	4.1	0.06	0.51	273	1.5	3.3	
10740	1746	132.1	0.6	298.4	0.3	0.09	0.16	276	3.8	0.05	0.26	278	1.5	3.4	

[a]Comments: 1, TES optical depths flagged as "questionable."

r_{eff} = 1.6 μm, and ±0.22 for r_{eff} = 2.3 μm. For v_{eff} = 0.1 (ice), an uncertainty of 15% produces ±0.3 μm for r_{eff} = 1.5 μm and an uncertainty of 10% gives ±0.35 for r_{eff} = 3.0 μm. Systematic effects in the data and, more importantly, in the model input parameters will tend to increase this uncertainty in a complex way, particularly for small aerosol columns. What is needed is a way to "calibrate" the scaling of the formal precision ($\sigma_{prec.}$) in a manner that adequately represents systematic effects in the retrieval process. In the interest of continuity, we list here only the end product of such a calibration. The details of the uncertainty estimates may be found in the Appendix. For dust, one finds $\sigma_{r,eff} \sim 0.15$ μm for $\tau_{dust} > 2.0$, 0.2 μm for $2.0 > \tau_{dust} > 1.0$, 0.2–0.3 μm for $1.0 > \tau_{dust} > 0.25$, and 0.3–0.5 μm for $0.25 > \tau_{dust} \gtrsim 0.1$; with uncertainty varying quasi-linearly between interval endpoints). Below $\tau_{dust} \sim 0.1$, the retrieval of r_{eff} is not particularly meaningful, having $\sigma_{r,eff} \sim 0.5$–1.0 μm. For water ice, we estimate $\sigma_{r,eff}$ as ~0.7–0.8 μm for $r_{eff} \sim 3$ μm and $\tau_{ice} \gtrsim 0.2$, but ~0.9–1.0 μm for $r_{eff} \sim 2.0$–2.5 μm and $\tau_{ice} \gtrsim 0.2$. For retrievals with $\tau_{ice} \lesssim 0.15$, our current algorithms cannot reliably distinguish between the two size ranges found in the larger τ_{ice} observations (i.e., 1.5–3.5 μm).

6.2. Automated Dust Storm Retrievals

[36] Numerical experimentation, using the results of the interactive analyses described above as a baseline, reveals that our automated algorithms handle dust retrievals reasonably well for the case of fixed ice particle sizes and $\tau_{dust} \gg \tau_{ice}$. In this light, we now present the results of two analyses which examine the temporal and spatial variability of dust optical depths and particle sizes during the course of the global dust storm 2001A. On the basis of the results from section 6.1 and those of Paper 1, we assume the presence of only Type 1 ice particles and set $r_{eff,ice}$ = 1.5 μm.

[37] Toward study of the dust temporal evolution, we construct a sample comprised of three small regions for a constant longitude range: a rectangle with dimensions 251°–259° W and 12°–8°S, which is northeast of the storm initiation point [*Smith et al.*, 2002]; and two regions further northward: 251°–259°W, 10°–12°N and 249°–261°W, 23°–27°N. We select all TES spectra which fall in the defined regions from shortly before the storm until well into its decay. The resulting data are binned by 1° in latitude to increase the signal-to-noise and to minimize surface emissivity variations in the data which fall below the resolution of our emissivity cube. These co-added spectra generally contain five individual integrations. The resulting retrievals are "filtered" by both χ^2 and T_{surf}. The "cut-off" values for each of the two criteria are set through the visual inspection of all model fits and the interactive retrieval of selected data points. For the three regions, a total of 101 model-fits survive the filtering process. The retrieved values are shown in Figures 10–14. The error bars represent the $\sigma_{r,eff}$ estimates, embodying both precision and accuracy terms, as described previously (section 6.1).

[38] In addition to the clear evidence for some temporal variations in r_{eff}, the data indicate a north-south gradient during the early part of the storm (smaller particles at more northerly latitudes). In order to investigate this further, we examine a second sample of very high optical depth observations which focus on latitudinal variations within specific longitude bins. We select TES spectra centered around four longitudes separated by ~90° near the peak of the 2001A storm (e.g., Figure 12) [see also *Smith et al.*, 2002]. The exact season chosen, L_S = 213°, is determined by the desire to compare with nearly contemporaneous Hubble Space Telescope optical images as part of a project to derive the visible scattering albedo (M. J. Wolff et al., manuscript in preparation, 2003). Using the same procedures adopted for the temporal analysis, we the derive r_{eff} values which are presented in Figures 15 and 16. Figures 17–19 provide the aerosol optical depths and T_{surf} associated with the r_{eff} fits of Figures 20 and 21.

7. Discussion

7.1. Particle Sizes

7.1.1. Comment on Model Dependence

[39] In addition to uncertainties discussed above, our use of specific dust/water ice dielectric functions and the

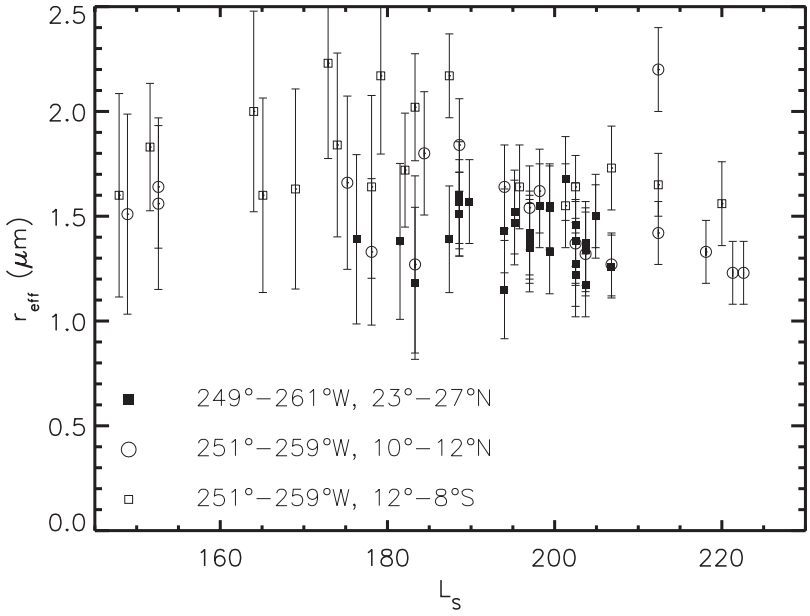

Figure 10. Sample of temporal variations in r_{eff} for $L_S = 145°–230°$ portion of dust storm 2001A. Three regions northeast and northward of the storm initiation point are examined. The error bars represent the estimates of $\sigma_{r,eff}$ as discussed in section 6.1. See text for more detail.

Bandfield [2002] surface emissivity spectra may contribute a potential bias in the absolute value of the r_{eff} derived. Due to the care taken in deriving emissivity spectra (e.g., omitting data with large amounts of aerosols) and our better understanding of water ice properties (relative to dust), any such effect would most likely be associated with the dust r_{eff}. However, the comparison to previous retrievals for low-to-moderate dust optical depths (see below) and to the values that are inferred from the visible-IR ratio of data in Table 1 (as well as for the water ice comparisons of Tables 2 and 3) lends considerable support to our model. In addition, systematic relative variations in r_{eff} would not contain a similar bias. That is to say, the observed statistically significant trends in particle size are model-independent; only their amplitude is sensitive the exact nature of our model dielectric function.

7.1.2. Water Ice

[40] Atmospheric water ice particle size retrievals are somewhat rare in the literature. In fact, direct measurement of r_{eff} through a combination of scattering and radiative

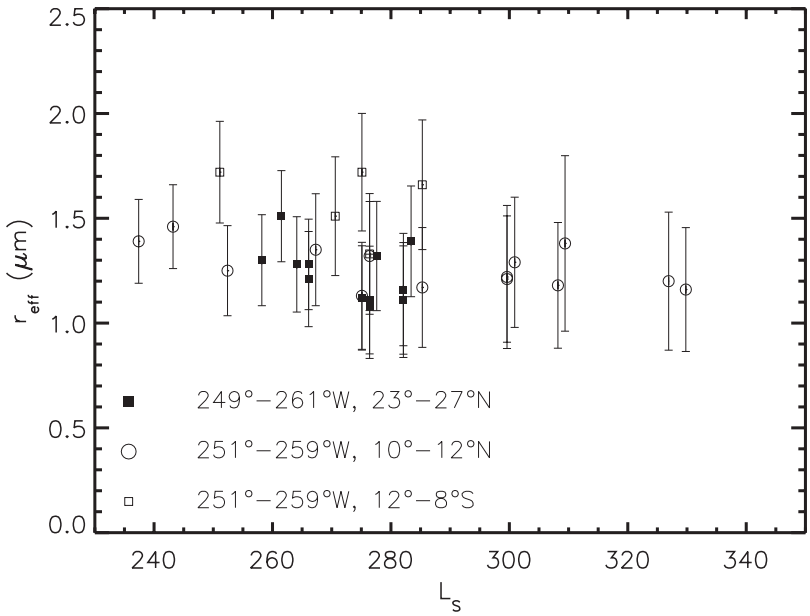

Figure 11. Sample of temporal variations in r_{eff} for $L_S = 230°–340°$ portion of dust storm 2001A. Details are the same as for Figure 10.

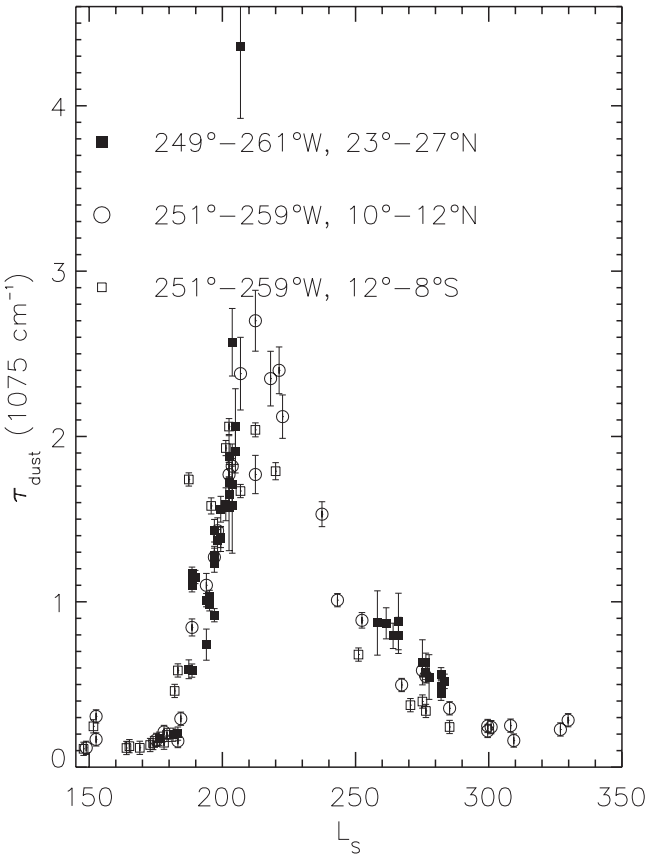

Figure 12. τ_{dust} values associated with the r_{eff} retrievals shown in Figures 10 and 11. The error bars represent the estimates of $\sigma_{\tau,eff}$ as discussed in section 6.1. See text for more detail.

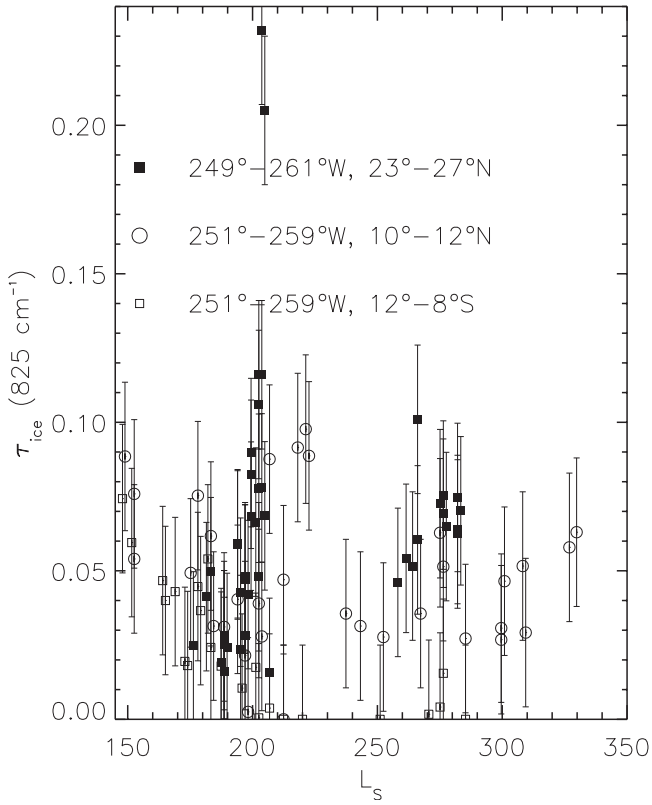

Figure 13. τ_{ice} values associated with the r_{eff} retrievals shown in Figures 10 and 11. Details are the same as for Figure 12.

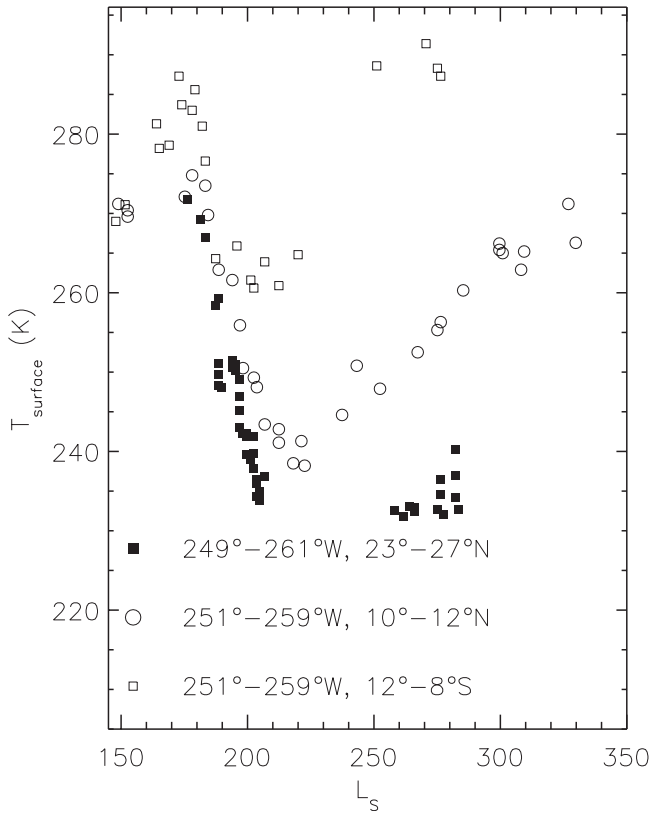

Figure 14. T_{surf} values associated with the r_{eff} retrievals shown in Figures 10 and 11. Details are the same as for Figure 12.

transfer analyses occurs in only a handful of refereed publications: *Curran et al.* [1973], *Petrova et al.* [1996], *Titov et al.* [1997], and *Montmessin et al.* [2002]. These authors arrive at r_{eff} = 2.2 μm, ≲1 μm, 0.7–1.0 μm, and 1.3–1.8 μm respectively. Although precision is either not reported or not well established in the aforementioned studies, our experience would indicate that one may view the reported values as being consistent with each other. A more indirect determination of r_{eff} = 2.3 μm is derived by *Rodin et al.* [1997] via a synthesis of Phobos data and a microphysical model. The seasons and locations sampled by the cited works correlate very well with our retrievals of similarly sized particles, namely those for our Type 1 ice cloud observations (see also Paper 1). Unfortunately, previous evidence of Type 2 water ice clouds is even scarcer than that for Type 1. In fact, other than preliminary results reported from our own current analyses [e.g., *Clancy et al.*, 2001; *Wolff et al.*, 2001], only *Glenar et al.* [2003] have previously reported statistically significant retrievals of the larger ice particle sizes. More specifically, *Glenar et al.* [2003] find their observations of the aphelion cloud belt during the 1999 season (L_S = 130°) to be consistent with *Clancy et al.* [2001]. In addition, although their size bins are quite coarse, they highlight systematic local time progression in particle sizes, from smaller particle sizes near 12:00 LST (∼2 μm) to larger ones (∼4 μm) by their final time step (∼15:00 LST).

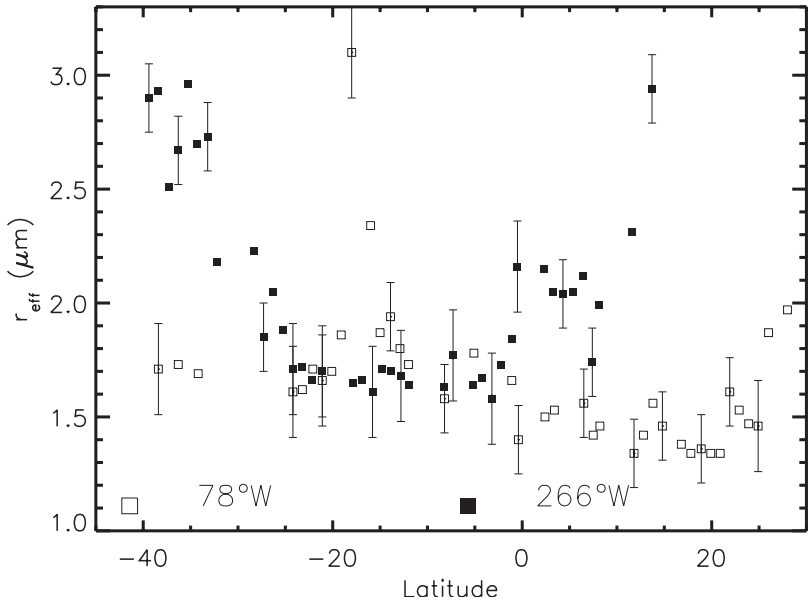

Figure 15. North-south retrievals of r_{eff} at $L_S = 213°$, near peak of dust storm 2001A. The spectra are taken from portions of TES orbits (ock number) 12554 and 12548, which have longitudes of 78° W and 266° W at the equator, respectively. The inclination of the orbital track is such that longitude varies about $\mp 4°$ from 40°S to 40°N. The error bars represent the estimates of $\sigma_{r,eff}$ as discussed in section 6.1. Only every third error bar is plotted. See text for more detail.

[41] The initial TES analysis of ice particle sizes by *Pearl et al.* [2001] yields an estimate of 2–4 μm which is implied to be applicable to water ice clouds in general, on the basis of an ice opacity shape that is "surprisingly invariant over time and space." However, this assertion has since been proven incorrect, as *Bandfield* [2002] derives a distinctly different "end-member" associated with the aphelion cloud belt. That is to say, the spectral shape employed by *Pearl et al.* [2001] is actually more appropriate for Type 1 clouds. In addition, inspection of Figure 5 of *Pearl et al.* [2001] shows that the 1 μm "model" appears to be of similar quality as that of the 2 μm case, while that for 4 μm is noticeably worse. Consequently, an $r_{eff} \sim 1–2$ μm provides a reasonable solution to their ice spectral fit, which would also be

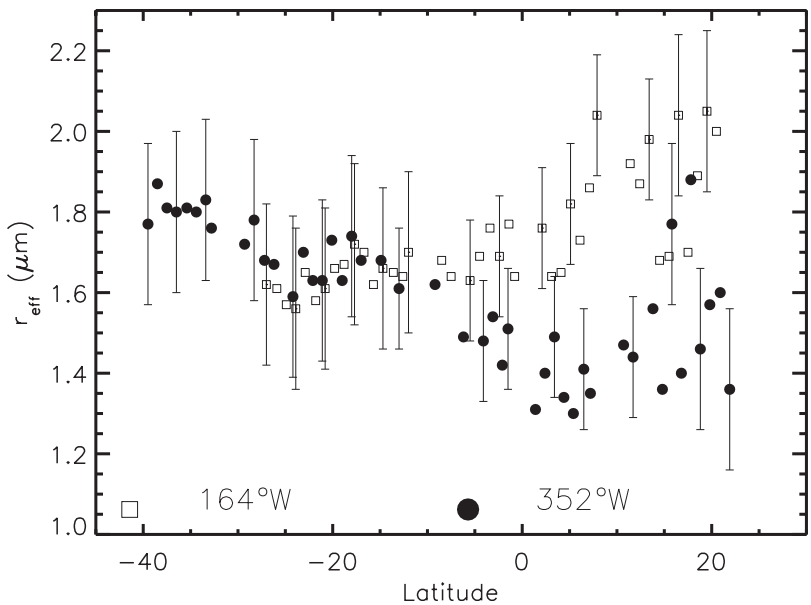

Figure 16. As for Figure 15, but the data are for portions of orbits (ock number) 12557 and 12551, with equator-crossing longitudes of 164°W and 352°W, respectively. Again, only every third error bar is plotted.

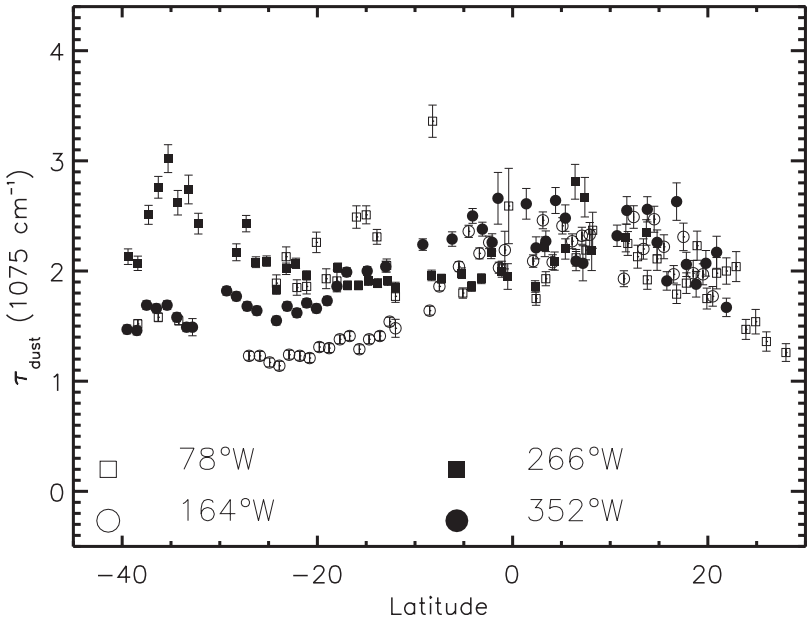

Figure 17. τ_{dust} values associated with the r_{eff} retrievals shown in Figures 15 and 16. The error bars represent the estimates of $\sigma_{\tau,eff}$ as discussed in section 6.1. See text for more detail.

consistent with interpretation of their adopted spectral shape as associated with Type 1 water ice clouds.

7.1.3. Dust

[42] Previous retrieval efforts of atmospheric dust particle sizes typically have focused on data sets which represent very limited seasonal/temporal domains [e.g., *Murphy et al.*, 1993; *Clancy et al.*, 1995; *Pollack et al.*, 1995; *Tomasko et al.*, 1999, and references within]. To the extent that our analyses overlap with the atmospheric conditions sampled by the cited studies of Mariner 9, Viking, and Pathfinder data, our results are certainly consistent with the r_{eff} = 1.6–1.8 μm values reported by the more recent papers [*Clancy et al.*, 1995; *Pollack et al.*, 1995; *Tomasko et al.*, 1999]. However, an important aspect of our work with respect to dust particle size lies in the demonstration that statistically significant variations, as a function of both time and space, do exist in r_{eff} (assuming a constant v_{eff} = 0.4). Although the uncertainties in r_{eff} for TES-based analyses of low-to-moderate optical depths cannot compete with the precision of the Pathfinder upward-viewing data set [*Tomasko et al.*, 1999], significant improvement is found in the case of larger dust loading levels (see section 6.1). In addition, the TES data set offers extensive temporal and spatial coverage of the Martian atmosphere. It is a combination of these two

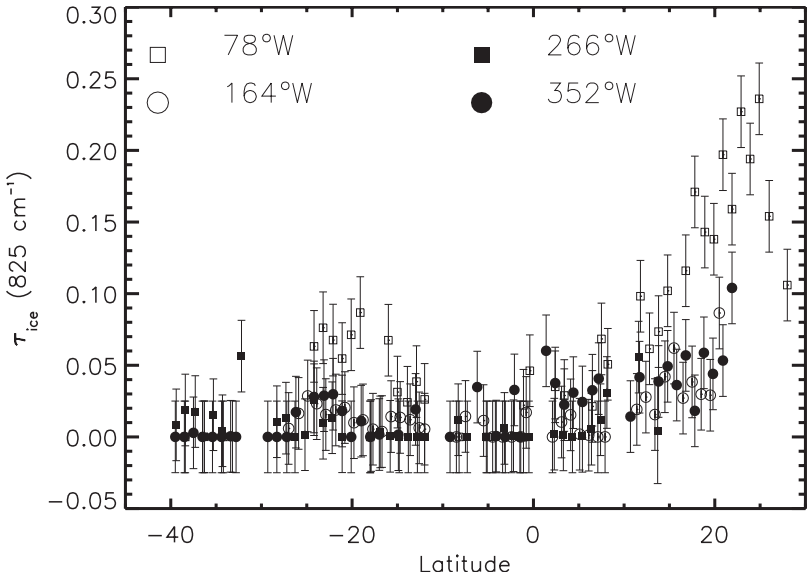

Figure 18. τ_{ice} values associated with the r_{eff} retrievals shown in Figures 15 and 16. Details are the same as for Figure 17.

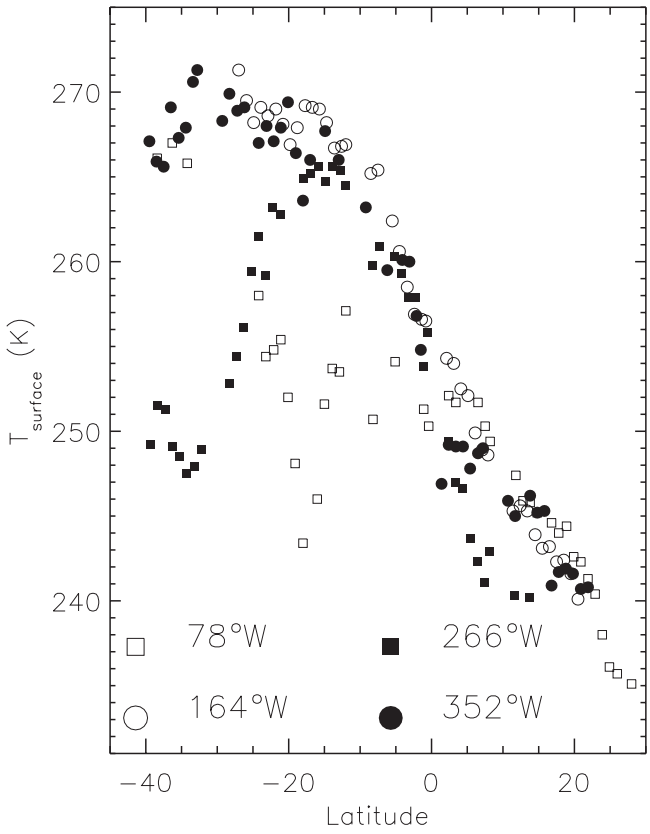

Figure 19. T_{surf} values associated with the r_{eff} retrievals shown in Figures 15 and 16. The errors are not plotted, but are described in section 6.1. Other details are as for Figure 17.

factors that provided us with the impetus to search for particle size variations associated with the 2001A global dust storm (i.e., section 6.2).

[43] The "interactive dust" GCM calculations of *Murphy et al.* [1993] provide a theoretical motivation for particle size changes associated with a global dust storm event. In particular, their analyses show clear spatial (including vertical) variations in dust particle sizes. Unfortunately, the zonally averaged nature of their results make comparison to our retrievals somewhat problematic; particularly when one considers the clearly delineated longitudinal variations presented in our retrievals (see Figures 15 and 16). Nevertheless, their work demonstrates the potentially important impact on atmospheric circulation due to the differences in atmospheric emissivity that would result from changes in r_{eff} (e.g., reduced cooling rates for smaller particles [see also *Haberle et al.*, 1982]). Furthermore, the presence of r_{eff} gradients in both latitude and longitude, at a variety of scale lengths, demonstrates the diagnostic capability of the TES data set for GCM and mesoscale models dust lifting/transport scheme, as well as for mapping of dust sources and sinks.

7.2. Comparison to TES Standard Retrievals

[44] The TES science team routinely derives aerosol optical depths and surface temperatures, in addition to vertical temperature profiles and other quantities, associated with each daytime nadir integration over non-ice covered surfaces. These data are delivered along with the calibrated radiances on a regular basis to the Planetary Data System (PDS) (see http://wufs.wustl.edu/missions/mgs/tes/index.html). Such τ_{dust}, τ_{ice}, and T_{surf} values are those to which we refer as being "TES team" or "PDS" retrievals. In some cases, we are using data that have not yet been delivered to PDS, but will be so available by the date of publication.

[45] The large volume of data required to be processed by the TES team for delivery, $\sim 10^8$–10^9 spectra thus far, necessitates extreme computational efficiency; especially relative to the computational effort involved in the retrievals presented here. As a result, a number of simplifying assumptions or approximations are made, including a purely absorbing atmosphere, a single surface emissivity shape, and a lack of iteration on T_{surf} [*Smith et al.*, 2000a, 2000b]. We consider these three approximate treatments to have the largest effect on our comparisons to the TES team processing and will discuss them in detail later. It is important to emphasize that sheer number of spectra preclude retrievals

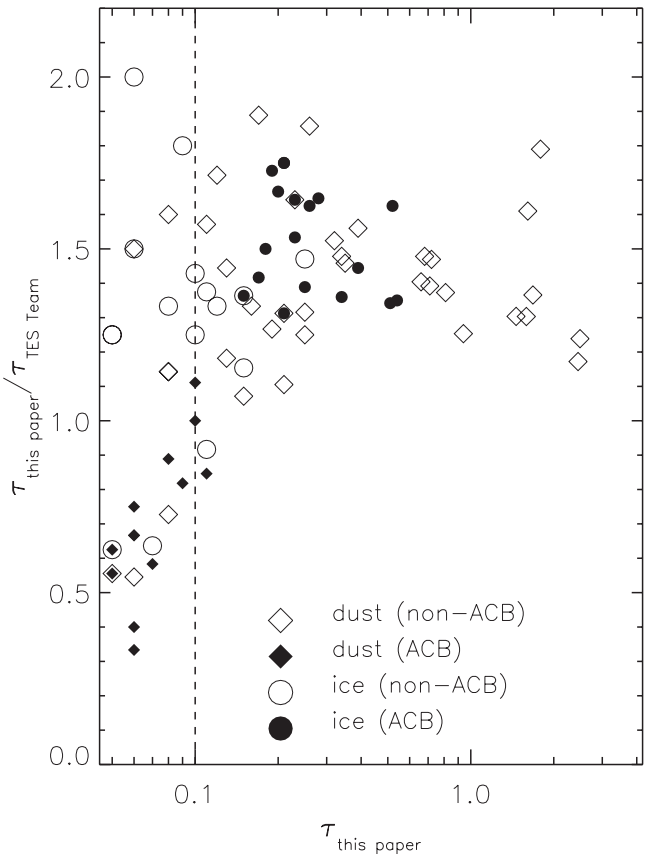

Figure 20. Comparison of our τ values to those provide to the PDS by the TES science team for the observations in Tables 1–3. ACB refers to observations over the "aphelion cloud belt," which may be typically be found in the 10°S–30°N latitude range during the $L_S \sim 50°$–$140°$ period. The dashed vertical line is drawn at $\tau = 0.1$ in order to approximate the transition between minor and major opacity components. That is to say, retrievals to the left of this line are typically those for the minor aerosol type. The "questionable" PDS retrievals are flagged in the tables.

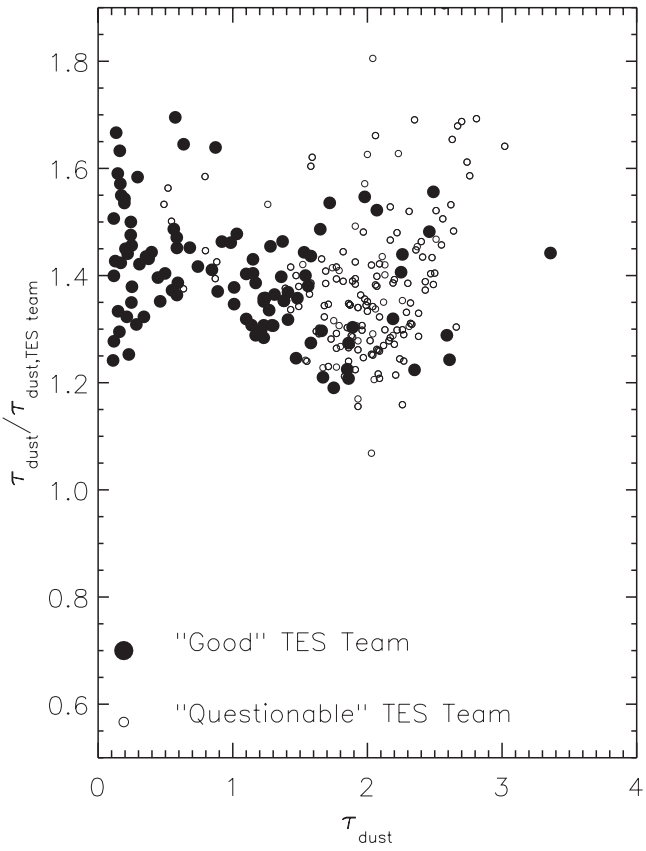

Figure 21. Comparison of our τ_{dust} values to those provide to the PDS by the TES science team for the two samples of focused global dust storm 2001A analyses of section 6.2. "Questionable" PDS optical depths are indicated by the open symbol type.

from being performed on the same number of spectra without the use of very similar or equivalent methods. That being said, it is reasonable to believe that such algorithms will introduce errors and uncertainty. The uncertainty in the TES/PDS (absorption) optical depths has not been well characterized; they are predicted to be underestimates of the true optical depths by 10–25% for low-to-moderate dust or water ice columns, and ~20% high dust opacities [*Bandfield et al.*, 2000; *Smith et al.*, 2000a, 2000b; *Bandfield and Smith*, 2003]. The more sophisticated, computational intensive numerical approach embodied in our retrievals would be expected to provide a more rigorous treatment of the processes involved, and consequently, a more representative set of values. Evidence of this expectation is provided by a comparison of our values to those found in the PDS AND by the subsequent accounting of the differences through an examination of the three assumptions of the TES team retrievals previously mentioned.

[46] Figures 20 and 21 directly compare our optical depths to the PDS values for our interactive survey (section 6.1) and focused dust storm (section 6.2) efforts, respectively (only τ_{dust} is included for the latter). Figure 22 presents differences in the respective deviations of T_{surf} as a function of τ_{dust}. The PDS values are flagged for cases when the TES team retrievals are not adequately able to fit the data. Among other things, a good retrieval is defined to exhibit $T_{surf} > 220$ *K*, $\tau > -0.05$ (i.e., a nonnegative opacity retrieval), and an optical depth fitting residual below a specified limit (M. Smith, 2003, private communication). The "questionable" retrievals included in our samples are flagged as a result of the latter two conditions; usually only a single criterion is violated. Not surprisingly, such flags occur for the more extreme values of τ_{dust} and τ_{ice}. Although the "flagged" symbols are preserved on the T_{surf} figure, the flag refers only to the opacity retrieval and is not a statement of quality regarding the surface temperature estimate.

[47] Inspection of these figures reveals several clear trends:

[48] 1. The previously reported 20–30% underestimation for PDS values of τ represents at best a lower limit to the observed ratio of optical depths. This is particularly true for the cases with a clearly dominant aerosol component (i.e., ACB water ice, or $\tau_{dust} \gtrsim 0.2$).

[49] 2. The presence larger particles will typically increase the τ ratios, especially as manifested in the ACB ice (filled circles) and, to a lesser extent, in the larger dust storm $r_{eff,dust}$ observations.

[50] 3. Underestimates of one component (e.g., ice) correspond to overestimates of the other (dust). This effect is one that can also be seen in the ACB retrievals - an

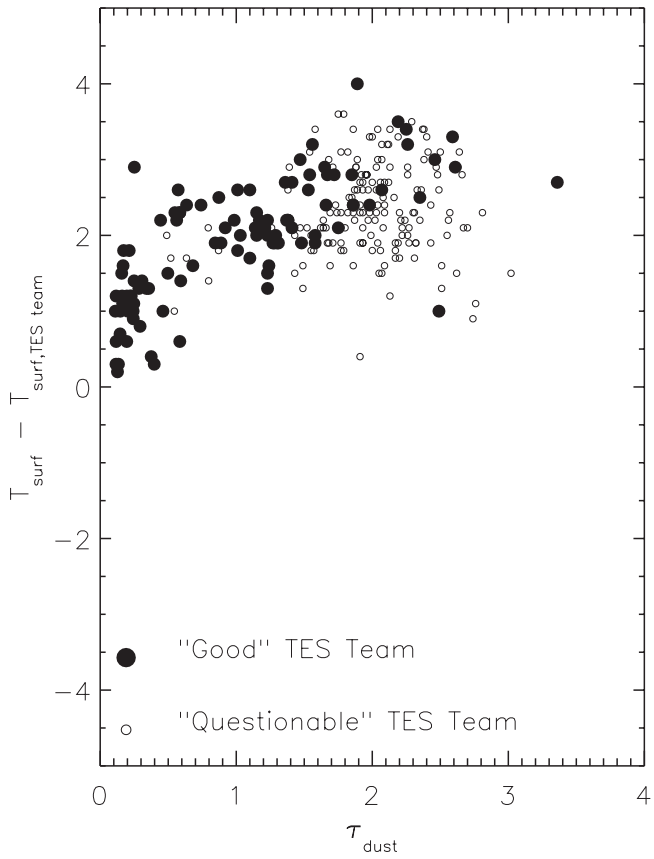

Figure 22. Comparison of our T_{surf} values to those provide to the PDS by the TES science team for two samples of focused global dust storm 2001A analyses of section 6.2. A "Questionable" PDS point indicates only a problematic opacity retrieval; it is not a quality flag for T_{surf}.

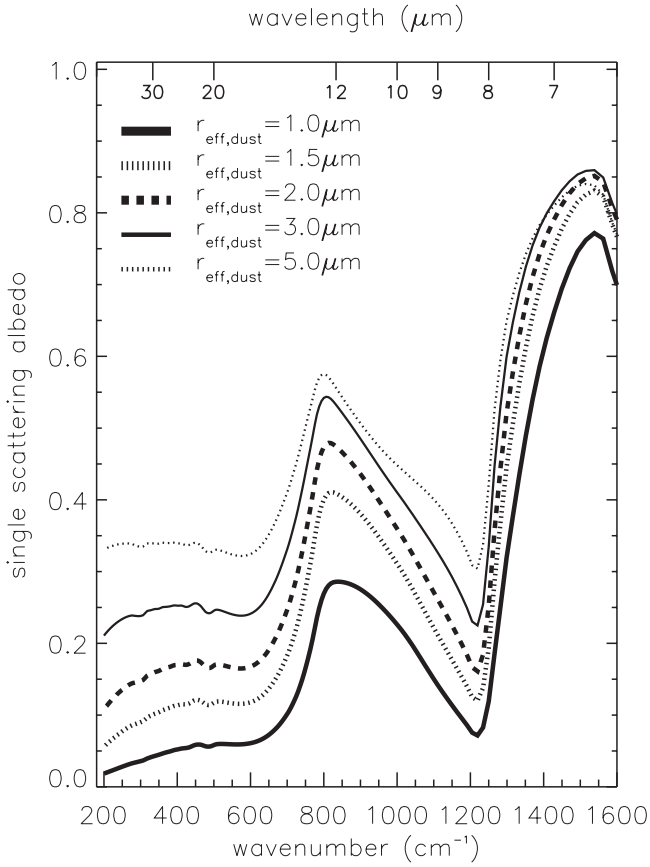

Figure 23. Single scattering albedo of our dust dielectric function across the TES spectral range. Several values of r_{eff} are shown under the assumption of $v_{eff} = 0.4$.

overestimate of ice and the presence of a "ghost" ACB in dust optical depths.

[51] 4. Significant scatter exists about the mean optical depth ratio of ~1.35, which correlates closely with the scatter seen in the T_{surf} differences.

[52] 5. A linear trend exists in the T_{surf} offsets as a function of τ. The amplitude of the differences, as well as much of the scatter, is dominated by the approximations intrinsic in the TES Team aerosol retrievals.

7.2.1. Purely Absorbing Atmosphere

[53] The use of a purely absorbing atmosphere makes the assumption that the single scattering albedo (ω) of any aerosols is "effectively" zero: i.e., $\tau_{extinction} \sim \tau_{absorption}$. The validity of the approximation hinges on both the departure of the actual aerosol ω values from zero and the relative contribution of scattered light. In other words, even for small ω this would clearly be a problem for limb retrievals, but might be adequate for analysis of nadir data. Figures 23 and 24 give the single scattering albedo values for our dust and ice models, respectively. Several r_{eff} calculations are shown in order to demonstrate of size-dependent effects. Although ω is small at the peak of the 1075 cm^{-1} and 825 cm^{-1} absorption features (which does not correspond with the minimum ω value), they are clearly nonzero, and the amplitude of the departure increases with r_{eff}. However, the fortuitous combination of low-to-moderate ω values (i.e., negligible multiple scattering), the extended nature of the emitting surface at nadir viewing, and the broad diffraction peak of the phase functions results in an effective (but not total) cancellation of scattering effects over much of the TES spectral range. That is to say, the amount of light scattered out of the field of view is roughly equivalent to that scattered into the field of view. This can be verified with simple radiative transfer calculations and has led to application of $\omega = 0$ models to many other thermal IR data sets [e.g., *Hanel et al.*, 1992]. So, despite the presence of significant scattering, absorption opacity calculations may well approximate the observed radiances.

[54] A large part of the comparative opacity ratio can simply be due to the fact that $\tau_{scattering}$ may be $\gtrsim 10-20\%$ of the total extinction despite the assumption of pure absorption. Ultimately, it is really a question of semantics, at least within the confines of optical depth determinations from TES data. The TES team algorithms provide $\tau_{absorption}$ while retrievals at optical and near-IR wavelengths are typically given in terms of total extinction. However, what appears to be often overlooked is that direct comparison of the two optical depths (i.e., the canonical VIS/IR ratio) is invalid without putting both in the same terms, either absorption or extinction. To the extent that one's ω values adequately represent the true functions, such a calculation is trivial: $\tau/\tau_{TES\ team} \sim \tau_{extinction}/\tau_{absorption} = 1/(1 - \omega)$. Averaging over a 100 cm^{-1} interval about the absorption

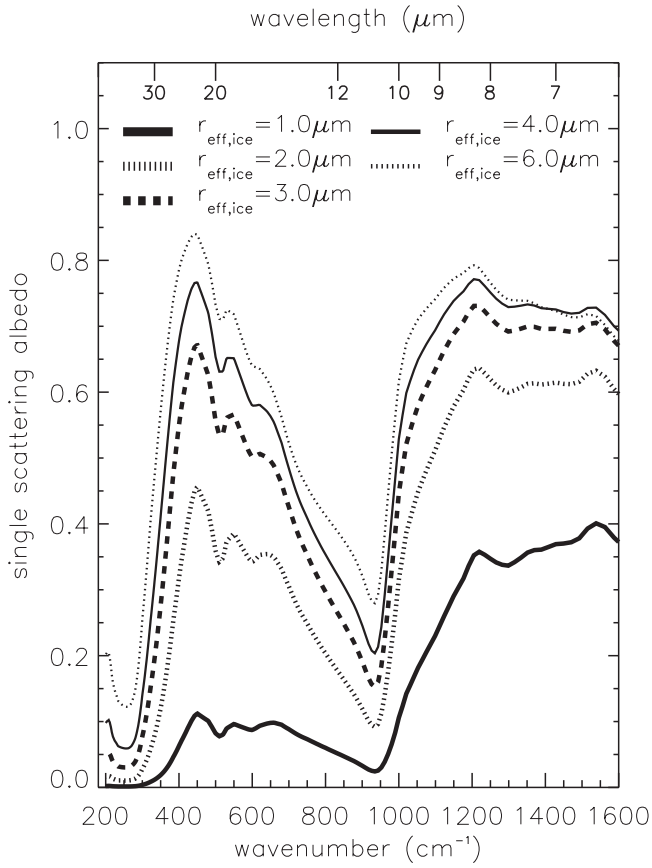

Figure 24. Single scattering albedo of the adopted water ice dielectric function across the TES spectral range. Several values of r_{eff} are shown under the assumption of $v_{eff} = 0.1$.

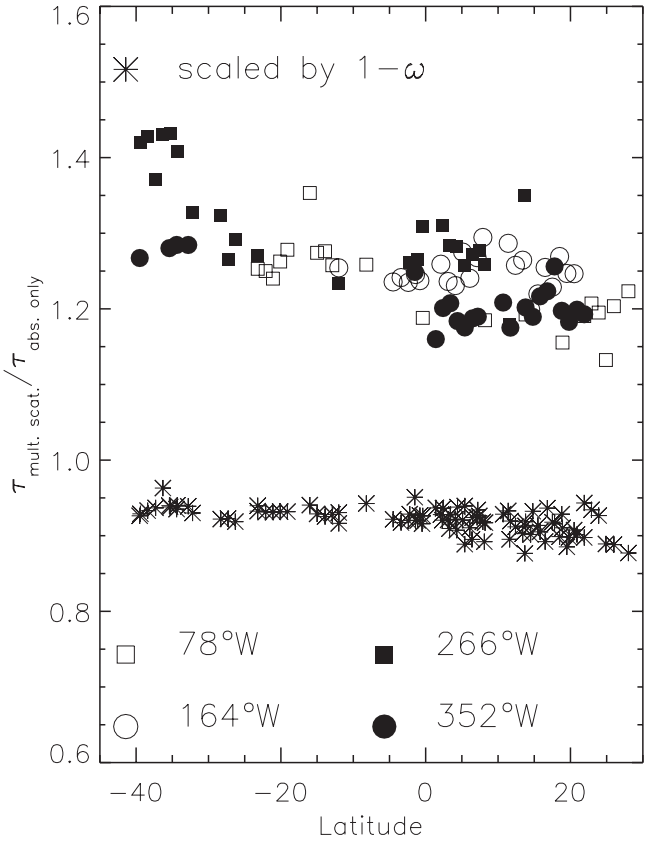

Figure 25. Comparison of τ_{dust} retrievals from the four north-south strips analyzed in section 6.2 with those derived from the same data under the assumption a purely absorbing atmosphere. Also shown is the result of applying the simple 1-ω correction/scaling (asterisk symbols). The quality of the model fits is generally worse in the pure absorption case for our model, with fewer points surviving the data quality "filtering" process.

feature centers, gives ω_{dust} = 0.17, 0.24, 0.29, 0.35, and 0.41 for r_{eff} = 1.0, 1.5, 2.0, 3.0 and 5.0 μm, respectively; and ω_{ice} = 0.054, 0.19, 0.28, 0.33, and 0.40 for r_{eff} = 1.0, 2.0, 3.0, 4.0, and 6.0 μm, respectively. Consequently, for the canonical $r_{eff,dust}$ = 1.5 and $r_{eff,ice}$ = 3.0 (ACB particles), we estimate $\tau/\tau_{TES\ team}$ to be 1.3 and 1.4, respectively. These values appear to be somewhat representative of the lower limits on the ratio values for Figures 20 and 21, though significant scatter is also apparent.

[55] In order to isolate the effect of the ω = 0 assumption, we re-analyze the four north-south strips from section 6.2 while explicitly setting $\tau_{scattering}$ and ω to zero after the Mie calculations are complete. Figure 25 shows the results in terms of optical depth retrieval ratios as was done for previous comparisons to the TES/PDS values. However, we also show the ratio when scaled by 1-ω, effectively comparing $\tau_{absorption}$ for both cases. The quality of the fits for the pure absorption model is typically worse and only about 60–70% of the re-analyzed data survive the same "quality filtering" as applied to the multiple-scattering retrievals. As can be clearly seen, the simple scaling removes the scatter induced by the r_{eff} sensitivity of ω although it "over-corrects" the $\tau_{extinction}$. In addition, a trend from south (∼1.3) to north (∼1.2) exists, which correlates with the systematically higher optical depths present in the northern part of the data set (see Figure 17). Ultimately, the departure from unity of the "corrected" retrievals is a simple illustration that the net effect of the scattering opacity is not precisely zero, and that its amplitude is a function of optical depth (among other variables).

7.2.2. Single Surface Shape

[56] The TES team optical depth retrieval process employs a single wavelength dependence or "shape" of the surface emissivity, which is representative of the typical southern hemisphere basaltic surface [*Bandfield et al.*, 2000; *Smith et al.*, 2000b]. Although the amplitude of the shape is allowed to vary, this prescription for emissivity is not generally adequate [e.g., *Bandfield*, 2002]. The competing effects of particle size and composition, as well as surface temperature errors, combine to prevent a simple characterization of the effects of the assumed surface emissivity on TES aerosol retrievals. Nevertheless, the implications are clear when one considers that a large fraction of the "questionable" symbols in Figures 21 and 22, particularly those which provide the "scatter," cluster geographically in regions for which the adopted shape is a poor description of the surface emissivity, e.g., northern hemisphere. While the identification of this correlation may be attributed to the larger optical depths, the fact remains that the PDS values of τ (and T_{surf} as well) manifest the potentially significant uncertainties associated with the assumption of a single surface emissivity description.

7.2.3. Lack of Iteration on T_{surf}

[57] In addition to the scatter that can be seen in Figure 22, a distinct linear trend with increasing τ_{dust} exists which is most clearly defined by the unflagged PDS values. This behavior is related to the neglect of atmospheric opacity. The TES team algorithm for T_{surf} selects the largest observed brightness temperature, typically near ∼1300 cm^{-1} [*Smith et al.*, 2000b; *Bandfield and Smith*, 2003]. The lack of iteration underestimates the resulting T_{surf} by an amount dependent on the optical depth at the chosen wavenumber, i.e., less atmospheric opacity becomes necessary to match the observed spectrum. This approximation leads to the observed trend of T_{surf}-$T_{surf,TES\ team}$ with τ. The impact of errors in T_{surf} on the PDS atmospheric opacity values are generally low-to-moderate in the aerosol band centers.

8. Conclusions

[58] We have employed a robust multiple-scattering radiative transfer algorithm in order to characterize the properties of Martian aerosol particles with respect to the MGS TES IR spectral data set. Our model included self-consistent and physically plausible treatments of surface emissivity and atmospheric aerosol dielectric functions, as well as treatment of gaseous absorption using correlated-k methodology. Considerable attention and effort was expended in the identification and discussion of the potential errors and uncertainties associated with our retrievals. Our work has presented the following:

[59] • A dust aerosol dielectric function is synthesized through the combination of previous work and of iterative adjustment using a variety of TES observations. The result-

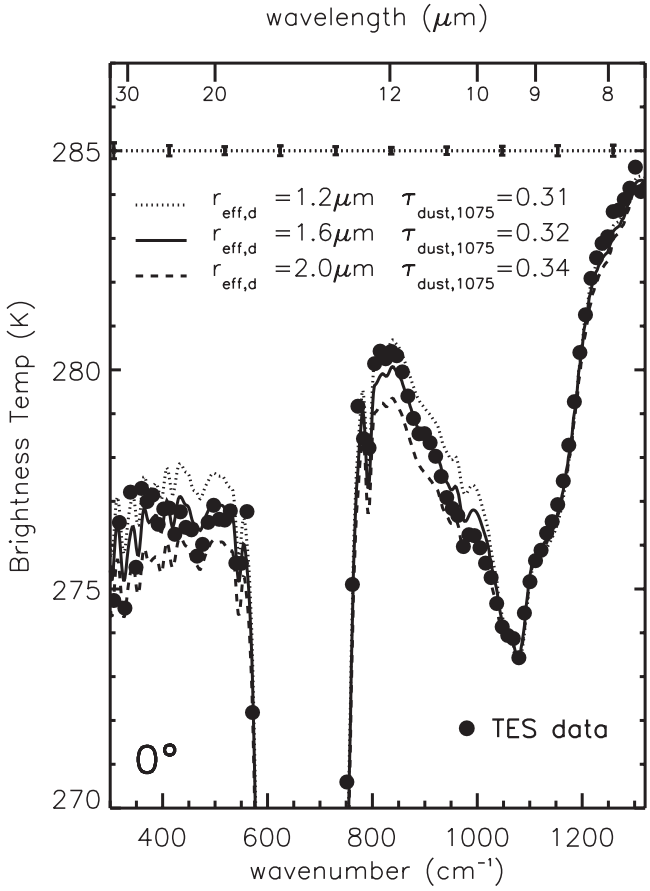

Figure 26. Model fits for the intermediate dust opacity case of ock 4279 (see Table 1). The error bars shown are intended to allow for the presence of additional (but unspecified) systematic error sources (see section 3). The best-fit model is compared with two models with r_{eff} values perturbed by twice our best estimate of the total uncertainty ($\sigma_{r,eff}$), which is approximately 3-$\sigma_{prec.}$. It is noteworthy that $\sigma_{r,eff} \sim$ 3-σ_{data}, as well. CO_2 and H_2O gaseous components are included, though the latter uses a zonally averaged value from *Smith* [2002]. No attempt was made to refine the H_2O column or to account for the wavenumber offsets between detectors which will significantly impact the model-data comparison in the 200–350 cm^{-1} range due to the "sharpness" of the lines [*Smith*, 2002].

ing function appears to well represent the IR spectral behavior sampled by TES for a wide range of dust loading conditions.

[60] ● The sensitivity of the TES spectral range to atmospheric particle size is demonstrated. While very little leverage exists to constrain v_{eff}, retrieval of r_{eff} is straightforward for both dust and water ice aerosols. Due to the partial masking of the 825 cm^{-1} (12 μm) ice feature by the main CO_2 absorption band and the problematic nature of the 250 cm^{-1} (40 μm) feature, the uncertainties related to $r_{eff,ice}$ can be appreciably larger than those for $r_{eff,dust}$.

[61] ● For our retrievals of $r_{eff,ice}$, we estimate the "effective" uncertainty or precision ($\sigma_{r,eff}$) as ∼0.7–0.8 μm for $r_{eff} \sim$ 3 μm and $\tau_{ice} \gtrsim$ 0.2, but ∼0.9–1.0 μm for $r_{eff} \sim$ 2.0–2.5 μm and $\tau_{ice} \gtrsim$ 0.2. For retrievals with $\tau_{ice} \lesssim$ 0.15, our current algorithms cannot reliably distinguish among the range of sizes found for the larger τ_{ice} observations (i.e., 1.5–3.5 μm).

[62] ● For our retrievals of $r_{eff,dust}$, we find $\sigma_{r,eff} \sim$ 0.15 μm for $\tau_{dust} >$ 2.0, 0.2 μm for 2.0 > $\tau_{dust} >$ 1.0, 0.2–0.3 μm for 1.0 > $\tau_{dust} >$ 0.25, and 0.3–0.5 μm for 0.25 > $\tau_{dust} \gtrsim$ 0.1; with uncertainty varying quasi-linearly between interval endpoints). Below $\tau_{dust} \sim$ 0.1, the determination of r_{eff} is not particularly meaningful, having $\sigma_{r,eff} \sim$ 0.5–1.0 μm.

[63] ● Two distinct populations of water ice particles are found in our retrievals: ∼1–2 μm and ∼3–4 μm. The former grouping is associated with TES solar band EPF definitions of Type 1 water ice clouds and the latter grouping with Type 2 clouds, which are temporally and spatially associated with the aphelion cloud belt (Paper 1). It is important to note the assignment of "ice types" is done here solely on the basis of the scattering phase function behavior as derived from the TES solar band EPF sequences of Paper 1. Hence agreement in correspondence of ice particle sizes and types between these companion studies provides independent corroboration.

[64] ● We find an average $r_{eff,dust}$ of 1.5–1.6 μm to be quite representative for low and moderate dust loading epochs; in agreement with the canonical 1.6–1.7 μm values

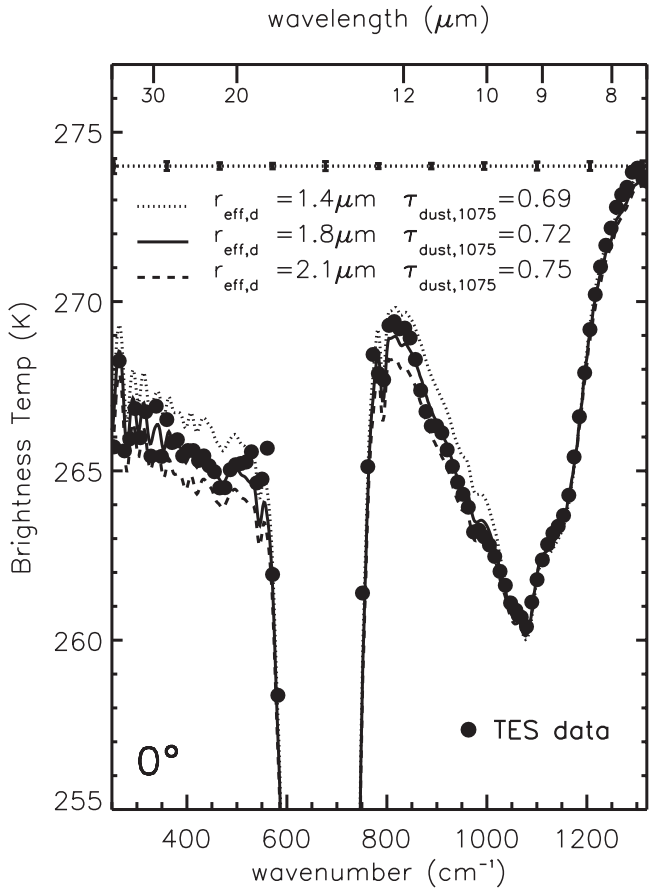

Figure 27. Model fits for the moderately high dust opacity case of ock 4545 (see Table 1). As for Figure 26, but now the best-fit model is compared to models with $r_{eff} \pm$ 2-$\sigma_{r,eff}$. Here, 2-$\sigma_{r,eff} \sim$ 2.5-$\sigma_{prec.} \sim$ 2.5σ_{data}.

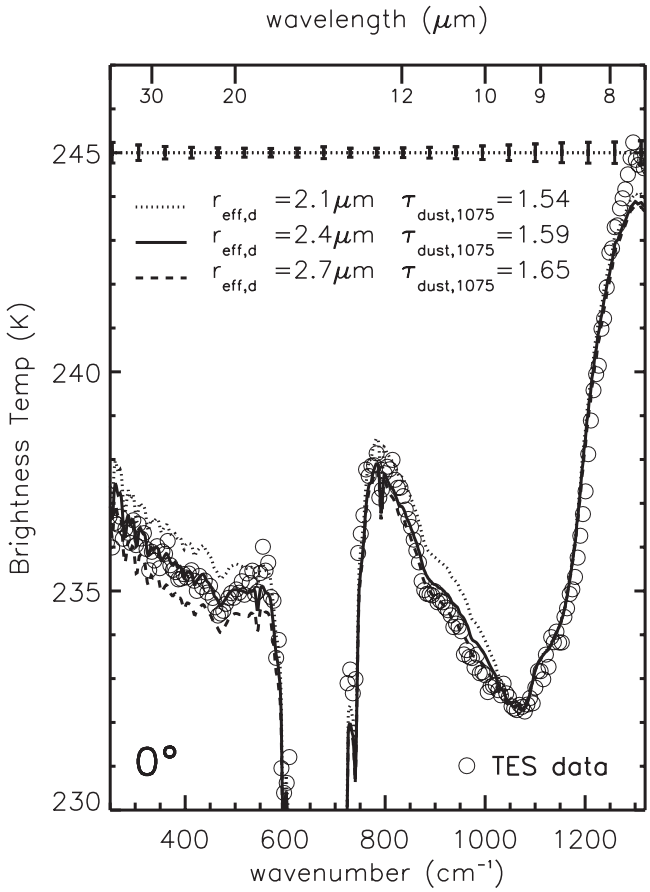

Figure 28. Model fits for the high opacity case (2001 global dust storm) of ock 12059 (see Table 1). As for Figure 26, but now 2-$\sigma_{r,eff} \sim$ 1.5-$\sigma_{prec.} \sim$ 1.5-σ_{data}.

found in the recent literature. However, distinct departures from can be seen in our sampling of the 2001A global dust storm. We find variations both above and below the average value. The presence of both latitudinal and longitudinal gradients in r_{eff} have potentially important implications for GCM and mesoscale models: e.g., changes in atmospheric cooling rates, diagnostic tracing of dust source and sinks, constraints on dust lifting and transport schemes.

[65] ● Direct comparison of our optical depths to those available the PDS (as provided by the TES science team) reveals an underestimate in the latter τ values by a minimum of 20–30%. The lower limit is essentially set by the fact the PDS provides an approximation of $\tau_{absorption}$ while our retrievals return $\tau_{extinction}$. Appreciable error (i.e., differences beyond the absorption versus extinction scaling) in the PDS values may also be present as a result of two assumptions employed by the nominal TES science team processing: a single surface emissivity shape and a fixed surface temperature. The former assumption, in particular, makes it difficult to derive an empirically corrected, accurate $\tau_{extinction}$ from the TES absorption optical depths.

[66] ● Comparison of our surface temperatures with in the PDS values also show systematic differences. As would be expected, a roughly linear trend with optical depth exists as a result of the fixed surface temperature assumption in the TES team processing. The significant scatter of the PDS T_{surf} around the linear behavior can be attributed in large part to the use of single surface emissivity shape.

Appendix A: Particle Size Uncertainty

[67] The connections between the formal precision and the effective retrieval uncertainty are empirically much more complicated for r_{eff} than for the other retrieved quantities. While one would hope that such contributions would be included, at least approximately, in the covariance matrix, we have not found this to be so. The independence in the TES wavenumber channels which is assumed in the formal statistical approach is not strictly valid for the fixed input parameters (i.e., dielectric functions, surface emissivity spectra, etc.). In other words, given the sensitivity of the r_{eff} determinations to the wavenumber dependence of the aerosol optical properties

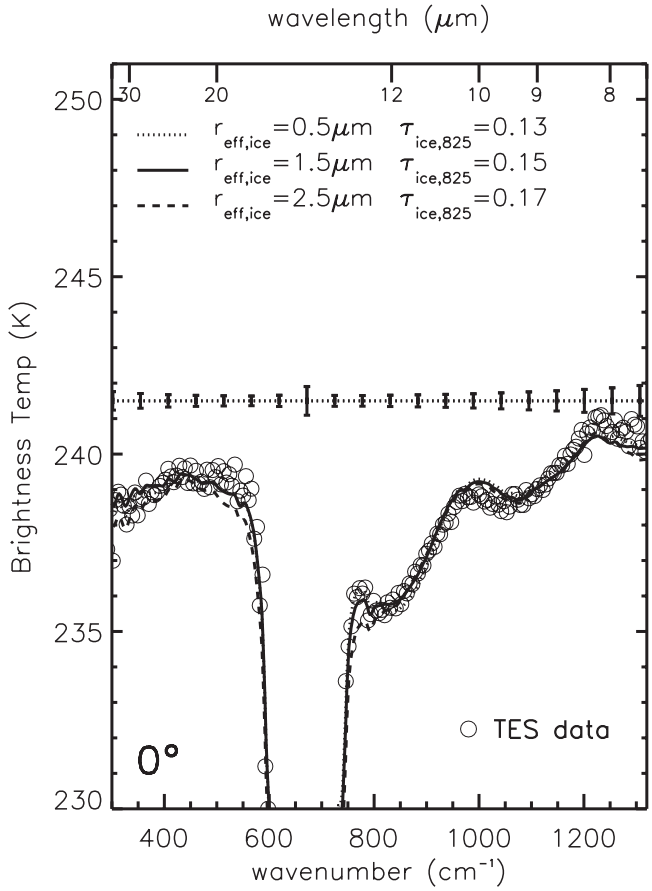

Figure 29. Model fits for the Type 1 ice particle case of ock 9929 (see Table 2). The best-fit model is compared to two r_{eff} values which demonstrate the difficulty in discriminating particle size variations for "small" ice grains. For the limited wavenumber ranges described in the text, the difference between the 1.5 μm and the estimated 1-$\sigma_{r,eff}$ upper bound of 2.5 μm models is ~3-$\sigma_{prec.}$ (but ~2-σ_{data}). However, no useful lower bound can be estimated solely with the use of these data. The model-data mismatch for 925–1050 cm^{-1} appears to be a systematic effect in the water ice dielectric function. CO_2, H_2O, and error bars are described in Figure 26.

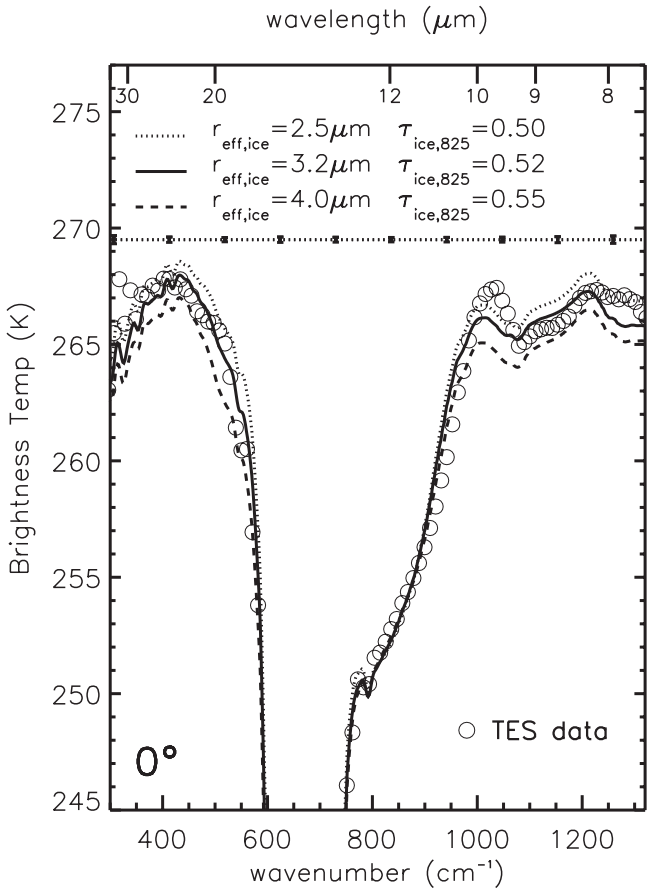

Figure 30. Model fits for the Type 2 ice particle case of ock 2420 (see Table 3). As for Figure 29, but the $r_{eff} \pm \sigma_{r,eff}$ models now represent 2-$\sigma_{prec.}$, but many-σ_{data}, perturbations. Due to the higher τ_{ice}, the suspected systematic effect in the ice dielectric function is more clearly seen (925–1050 cm^{-1}). See text.

and surface emissivity between the critical shortwave absorption features and the longwave continuum region (e.g., Figures 6 and 9), the method used above for calculating $\sigma_{prec.}$ assumes a lack of correlation between TES channels that does not exist. Basically, this causes the calculation of $\sigma_{prec.}$ to be drastically underestimated. As before, we employ brute-force numerical experimentation to estimate $\sigma_{r,eff}$, with an emphasis on the sensitivity of r_{eff} retrievals to systematic errors in τ and T_{surf}.

[68] For dust, Figures 26–28 illustrate the connection between $\sigma_{r,eff}$ and $\sigma_{prec.}$. Not surprisingly, the larger optical depths show a diminished sensitivity to systematic effects, as evidenced by the decrease in the scale factor between $\sigma_{r,eff}$ and $\sigma_{prec.}$. The correspondence of σ_{data} and $\sigma_{prec.}$ does provide an indication of the potential applicability of a more automated approach. Extending our "calibration" to all the retrievals in Tables 1–3, one finds $\sigma_{r,eff} \sim 0.15$ μm for $\tau_{dust} > 2.0$, 0.2 μm for $2.0 > \tau_{dust} > 1.0$, 0.2–0.3 μm for $1.0 > \tau_{dust} > 0.25$, and 0.3–0.5 μm for $0.25 > \tau_{dust} \gtrsim 0.1$; with uncertainty varying quasi-linearly between interval endpoints). Below $\tau_{dust} \sim 0.1$, the retrieval of r_{eff} is not particularly meaningful, having $\sigma_{r,eff} \sim 0.5$–1.0 μm.

[69] Unfortunately, the case for water ice is more problematic. Since we are forced to exclude the 250 cm^{-1} (40 μm) absorption feature due to instrumental issues (e.g., poor signal-to-noise) and the lack of accurate surface emissivity data [*Bandfield*, 2002], very little diagnostic power for r_{eff} is available outside of the 825 cm^{-1} absorption feature (see Figures 6 and 7). This is particularly true for $r_{eff} < 2.0$ μm where one finds a reduced "size-contrast" of the particle scattering cross sections, i.e., nearly size-independent Rayleigh-like scattering behavior. Furthermore, a large part of the 825 cm^{-1} feature is "obscured" by the 667 cm^{-1} CO_2 band. Nevertheless, as can be seen in Figures 29 and 30, one may discriminate between small ice ($r_{eff} < 2$ μm) and large ice ($r_{eff} > 2.5$ μm) particles through a combination of the 750–825 cm^{-1} and 400–550 cm^{-1} regions. The relationship between $\sigma_{prec.}$ and our estimates of $\sigma_{r,eff}$ is similar to that for dust, with the scale factor decreasing as optical depth and particle size increase. However, the particle size is now a more dominant influence due to the larger sizes now present: 3–4 μm versus ~2 μm for dust (see also Figures 6 and 9). For the values of $r_{eff,ice}$ in Tables 1–3, we estimate $\sigma_{r,eff}$ as ~0.7–0.8 μm for $r_{eff} \sim 3$ μm and $\tau_{ice} \gtrsim 0.2$, but ~0.9–1.0 μm for $r_{eff} \sim 2.0$–2.5 μm and $\tau_{ice} \gtrsim 0.2$. For retrievals with $\tau_{ice} \lesssim 0.15$, our current algorithms cannot reliably distinguish among the range of sizes found for the larger τ_{ice} observations (i.e., 1.5–3.5 μm).

[70] It is worthwhile to briefly mention the model-data mismatch in the 925–1050 cm^{-1} range. It appears to be intrinsic to the adopted water ice dielectric function (see section 4.4). The scaling of its amplitude with optical depth and its absence in dusty spectra over the same regions would indicate that it is not an artifact of the data or of the adopted emissivity spectra. Variations in particle shape (spheroids, cylinders) and aspect ratio produce only negligible changes to particle cross sections in this size parameter regime. In other words, terrestrial measurements of "Ice 1h" cannot completely reproduce the behavior of Martian ice particles, at least with respect to the wavenumber region in question. While this undoubtedly contributes to the large amplitude of $\sigma_{r,eff}$ as well as to the "disconnection" between $\sigma_{prec.}$ and σ_{data}, we leave the resolution of this issue to a later effort.

[71] **Acknowledgments.** We very grateful for the excellent support provided by the TES operations team, especially Kelly Bender and Kim Murray. We thank Joshua Bandfield and Michael Smith for providing helpful discussions and derived data products. The software and data contributions of Kelly Snook, Gary Hansen, Michael Mishchenko, Warren Wiscombe, and their collaborators were invaluable in the completion of our work. This manuscript was improved through the constructive reviews of David Glenar and an anonymous referee. We acknowledge the support of the Mars Data Analysis Program under grants NAG5-9820 (MJW) and NAG5-10662 (RTC).

References

Bandfield, J. L., Global mineral distribution on Mars, *J. Geophys. Res.*, *107*(E6), 5042, doi:10.1029/2001JE001510, 2002.

Bandfield, J. L., and M. D. Smith, Multiple emission angle surface-atmosphere separations of Thermal Emission Spectrometer, *Icarus*, *161*(1), 47–65, 2003.

Bandfield, J. L., P. R. Christensen, and M. D. Smith, Spectral data set factor analysis and end-member recovery: Application to analysis of Martian atmospheric particulates, *J. Geophys. Res.*, *105*, 9573–9588, 2000.

Bohren, C. F., and D. R. Huffman, *Absorption and Scattering of Light by Small Particles*, John Wiley, New York, 1983.

Christensen, P. R., et al., Mars Global Surveyor Thermal Emission Spectrometer experiment: Investigation description and surface science results, *J. Geophys. Res.*, *106*(E10), 23,823–23,871, 2001.

Clancy, R. T., and S. W. Lee, A new look at dust and clouds in the Mars atmosphere: Analysis of emission-phase-function sequences from global Viking IRTM observations, *Icarus*, *93*, 135–158, 1991.

Clancy, R. T., S. W. Lee, G. R. Gladstone, W. W. McMillan, and T. Rousch, A new model for Mars atmospheric dust based upon analysis of ultraviolet through infrared observations from Mariner 9, Viking, and Phobos, *J. Geophys. Res.*, *100*, 5251–5264, 1995.

Clancy, R. T., A. W. Grossman, M. J. Wolff, P. B. James, D. J. Rudy, Y. N. Billawala, B. J. Sandor, S. W. Lee, and D. O. Muhleman, Water vapor saturation at low altitudes around aphelion: A key to Mars climate?, *Icarus*, *122*, 36–62, 1996.

Clancy, R. T., M. J. Wolff, and P. R. Christensen, Types, sizes, shapes and distributions of mars ice and dust aerosols from the MGS TES emission phase function observations, *Eos Trans. AGU*, *82*(47), Fall Meet. Suppl., abstract P42A-0542., 2001.

Clancy, R. T., M. J. Wolff, and P. R. Christensen, Mars aerosol studies with the MGS TES emission phase function observations: Optical depths, particle sizes, and ice cloud types versus latitude and solar longitude, *J. Geophys. Res.*, *108*, doi:10.1029/2003JE002058, in press, 2003.

Conrath, B. J., Thermal structure of the Martian atmosphere during the dissipation of the dust storm of 1971, *Icarus*, *24*, 36–46, 1975.

Conrath, B. J., J. C. Pearl, M. D. Smith, W. C. Maguire, P. R. Christensen, S. Dason, and M. S. Kaelbererr, Mars Global Surveyor Thermal Emission Spectrometer (TES) observations: Atmospheric temperatures during aerobraking and science phasing, *J. Geophys. Res.*, *105*, 9509–9520, 2000.

Curran, R. J., B. J. Conrath, R. A. Hanel, V. G. Kunde, and J. C. Pearl, Mars: Mariner 9 spectroscopic evidence for H_2O ice clouds, *Science*, *182*, 381–383, 1973.

Deirmidjian, D., Scattering and polarization properties of water clouds and hazes in the visible and infrared, *Appl. Opt.*, *3*, 187–202, 1964.

French, R. G., P. J. Gierasch, B. D. Popp, and R. J. Yerdon, Global patterns in cloud forms on Mars, *Icarus*, *45*, 468–493, 1981.

Gierasch, P. J., and R. M. Goody, The effect of dust on the temperature structure of the Martian atmosphere, *J. Atmos. Sci.*, *29*, 400–402, 1972.

Gladstone, G. R., J. W. Kaminski, R. Link, and J. C. McConnell, Cloud radiance modeling: Phase II, *Contract KM147-4-1041*, Can. Dept. of the Environ., Ottawa, Ontario, Canada, 1984.

Glenar, D., R. E. Samuelson, J. C. Pearl, G. L. Bjoraker, and D. Blaney, Spectral imaging of Martian water ice clouds and their diurnal behavior during the 1999 aphelion season (LS = 130°), *Icarus*, *161*, 297–318, 2003.

Haberle, R. M., C. B. Leovy, and J. B. Pollack, Some effect of global dust storms on the atmospheric circulation of Mars, *Icarus*, *50*, 322–367, 1982.

Hanel, R. A., B. J. Conrath, D. E. Jennings, and R. E. Samuelson, *Exploration of the Solar System by Infrared Remote Sensing*, Cambridge Univ. Press, New York, 1992.

Hansen, J. E., and L. D. Travis, Light scattering in planetary atmospheres, *Space Sci. Rev.*, *16*, 527–610, 1974.

Hapke, B., *Theory of Reflectance and Emittance Spectroscopy*, Cambridge Univ. Press, New York, 1993.

Hapke, B., A model of radiative and conductive energy transfer in planetary regoliths, *J. Geophys. Res.*, *101*(E7), 16,817–16,832, 1996.

Jakosky, B. M., G. W. Finiol, and B. G. Henderson, Directional variations in thermal emission from geologic surfaces, *Geophys. Res. Lett.*, *17*, 985–988, 1990.

Lacis, A. A., and V. Oinas, A description of the correlated k distribution method for modeling nongray gaseous absorption, thermal emission, and multiple scattering in vertically inhomogeneous atmosphere, *J. Geophys. Res.*, *96*, 9027–9063, 1991.

Mishchenko, M. I., L. D. Travis, and D. W. Mackowski, *J. Quant. Spectrosc. Radiat. Transfer*, *55*, 535–575, 1996.

Montmessin, F., P. Rannou, and M. Cabane, New insights into Martian dust distribution and water-ice cloud microphysics, *J. Geophys. Res.*, *107*(E6), 5037, doi:10.1029/2001JE001520, 2002.

Moré, J. J., D. C. Sorensen, K. E. Hillstrom, and B. S. Garbow, The MINPACK Project, in *Sources and Development of Mathematical Software*, edited by W. J. Cowell, Prentice-Hall, Old Tappan, N. J., 1984.

Murphy, J. R., R. M. Haberle, O. B. Toon, and J. B. Pollack, Martian global dust storms: Zonally symmetric numerical simulations including size-dependent particle transport, *J. Geophys. Res.*, *98*, 3197–3220, 1993.

Ockert-Bell, M. E., J. F. Bell III, J. B. Pollack, C. P. McKay, and F. Forget, *J. Geophys. Res*, *102*, 9039–9050, 1997.

Pang, K., J. M. Ajello, C. W. Hord, and W. G. Egan, Complex refractive index of Martian dust: Mariner 9 ultraviolet observations, *Icarus*, *27*, 55–67, 1976.

Pearl, J. C., M. D. Smith, B. J. Conrath, J. L. Bandfield, and P. R. Christensen, Observations of Martian ice clouds by the Mars Global Surveyor Thermal Emission Spectrometer: The first year, *J. Geophys. Res.*, *106*, 12,325–12,338, 2001.

Petrova, E. H., U. Keller, W. J. Markiewicz, N. Thomas, and M. W. Wuttke, Ice hazes and clouds in the Martian atmosphere as derived from the Phobos/KRFME data, *Planet. Space Sci.*, *44*, 1163–1176, 1996.

Pitman, K. M., M. J. Wolff, J. L. Bandfield, R. T. Clancy, and G. C. Clayton, Directional emissivity effects on Martian surface brightness temperatures, *Bull. Am. Astron. Soc*, *33*, 36.01, 2001.

Pollack, J. B., D. Hollenbach, S. Beckwith, D. P. Simonelli, T. Roush, and W. Wesley, Composition and radiative properties of grains in molecular clouds and accretion disks, *Astrophys. J.*, *421*, 615–639, 1994.

Pollack, J. B., M. E. Ockert-Bell, and M. K. Sheppard, Viking lander analysis of Martian atmospheric dust, *J. Geophys. Res.*, *100*, 5235–5250, 1995.

Rodin, A. V., O. I. Korablev, and V. I. Moroz, Vertical distribution of water in the near-equatorial troposphere of Mars: Water vapor and clouds, *Icarus*, *125*, 212–229, 1997.

Roush, T., J. Pollack, and J. Orenberg, Derivation of midinfrared (5–25 microns) optical constants of some silicates and palagonite, *Icarus*, *94*, 191–208, 1991.

Smith, D. E., et al., Mars Orbiter Laser Altimeter: Experiment summary after the first year of global mapping of Mars, *J. Geophys. Res.*, *106*(E10), 23,689–23,722, 2001.

Smith, M. D., Annual cycle of water vapor on Mars as observed by the Thermal Emission Spectrometer, *J. Geophys. Res.*, *107*(E11), 5115, doi:10.1029/2001JE001522, 2002.

Smith, M. D., J. C. Pearl, B. J. Conrath, and P. R. Christensen, Mars Global Surveyor Thermal Emission Spectrometer (TES) observations of dust opacity during aerobraking and science phasing, *J. Geophys. Res.*, *105*, 9539–9552, 2000a.

Smith, M. D., J. L. Bandfield, and P. R. Christensen, Separation of atmospheric and surface spectral features in Mars Global Surveyor Thermal Emission Spectrometer (TES) spectra, *J. Geophys. Res.*, *105*, 9589–9608, 2000b.

Smith, M. D., B. J. Conrath, J. C. Pearl, and P. R. Christensen, Thermal Emission Spectrometer observations of Martian planet-encircling dust storm 2001A, *Icarus*, *157*, 259–263, 2002.

Smith, P. H., and M. Lemmon, Opacity of the Martian atmosphere measured by the Imager for Pathfinder, *J. Geophys. Res.*, *104*, 135–158, 1999.

Smith, S. A., and B. A. Smith, Diurnal and seasonal behavior of discrete white clouds on Mars, *Icarus*, *16*, 509–521, 1972.

Snook, K. J., Optical properties and radiative heating effects of dust suspended in the Mars atmosphere, Ph.D thesis, Stanford Univ., Stanford, Calif., 1999.

Snook, K. J., J. L. Bandfield, F. Forget, and C. P. McKay, Derivation of infrared optical properties of dust suspended in the Martian atmosphere from MGS-TES data, *Bull. Am. Astron. Soc*, *32*, 51.08, 2000.

Tamppari, L. K., R. W. Zurek, and D. A. Paige, Viking era water ice clouds, *J. Geophys. Res.*, *105*, 4087–4107, 2000.

Titov, D. V., V. I. Moroz, and Y. M. Getkin, Aerosol component of the Martian atmosphere and its variability from the results of infrared radiometry in the Termoscan/Phobos-2 Experiment, *Planet. Space Sci.*, *45*, 637–651, 1997.

Toigo, A. D., and M. I. Richardson, Seasonal variations of aerosols in the Martian atmosphere, *J. Geophys. Res.*, *105*, 4109–4121, 2000.

Tomasko, M. G., L. R. Doose, M. Lemmon, E. Wegryn, and P. H. Smith, Properties of dust in the Martian atmosphere from the imager on Mars Pathfinder, *J. Geophys. Res.*, *104*, 8987–9008, 1999.

Toon, O. B., J. B. Pollack, and C. Sagan, Physical properties of the particles composing the Martian dust storm of 1971, *Icarus*, *30*, 663–696, 1977.

Warren, S., Optical constants of ice from the ultraviolet to the microwave, *Appl. Opt.*, *23*, 1206–1225, 1984.

Wehrli, C., (Ed.), *Extraterrestrial Solar Spectrum*, *Publ. 615*, Phys. Metereol. Observ., Davos Dorf, Switzerland, July 1985.

Wehrli, C., (Ed.), *World Climate Research Programme*, *Publ. Ser. 7, WMO ITD 149*, pp. 119–126, World Meteorol. Organ., Geneva, Switzerland, Oct. 1986.

West, R. A., Optical properties of aggregate particles whose outer diameter is comparable to the wavelength, *Appl. Opt.*, *30*, 5316–5324, 1991.

Wolff, M. J., R. T. Clancy, K. M. Pitman, P. R. Christensen, and B. A. Whitney, Mars aerosol studies with the MGS TES emission phase function observations: Opacities, particle sizes, and ice cloud types, *Bull. Am. Astron. Soc*, *33*, 34.06, 2001.

R. T. Clancy and M. J. Wolff, Space Science Institute, 3100 Marine Street, Suite A353, Boulder, CO 80303-1058, USA. (clancyr@colorado.edu; wolff@colorado.edu)